International Journal of Mechanical Sciences 218 (2022) 107044

Contents lists available at ScienceDirect

International Journal of Mechanical Sciences

journal homepage: www.elsevier.com/locate/ijmecsci

Optimal negative stiffness inertial-amplifier-base-isolators: Exact closed-form expressions

S. Chowdhury [a], A. Banerjee [a,*], S. Adhikari [b]

[a] Civil Engineering Department, Indian Institute of Technology Delhi (IITD), India
[b] James Watt School of Engineering, The University of Glasgow, Glasgow, UK

ARTICLE INFO

Keywords:
Novel isolator
Negative stiffness
inertial-amplifier-base-isolators
IABI
NSIABI
NSBI
TBI
Mass tuning ratio

ABSTRACT

This paper introduces the concept of negative stiffness inertial-amplifier-base-isolators to achieve enhanced broadband vibration control. Three physically different novel isolators, namely inertial amplifier base isolator (IABI), negative stiffness inertial amplifier base isolator (NSIABI), and negative stiffness base isolator (NSBI), are achieved only by tuning a single system parameter, namely the mass tuning ratio for novel isolators γ. The exact closed-form expressions for the optimal system parameters, such as the frequency and damping ratio of the novel isolators, have been derived analytically using H_2 and H_∞ optimization methods. The response reduction capacity of each optimized novel isolator has been compared with the optimized traditional base isolator (TBI). Results showed that the vibration reduction capacity of H_2 optimized NSBI, NSIABI, and IABI is significantly 73.02%, 75.55%, and 76.48 %, superior to the TBI. While, the vibration reduction capacity of H_∞ optimized NSBI, NSIABI, and IABI is significantly 69.69%, 73.67%, and 77.37% superior to the TBI. Overall all three novel base isolators have at least 69% more vibration reduction capacity than traditional base isolators, respectively. These novel isolators are cost-effective and can provide superior vibration reduction capacity than other existing traditional base isolators, respectively.

1. Introduction

Since Touaillon's isolation mechanism [1] in 1870, base isolation devices have become the most widely acclaimed vibration control device studied and implemented in several fields in mechanical and civil engineering, from vehicle suspension system [2–8] to liquid storage tank [9–13], building [14], bridges, aircraft landing gear [15], etc. Base isolation devices are implemented in structures to decouple the superstructure [16,17] from the base during any seismic events, targeting to minimize the inter-story drift and accelerations by implanting it between the structure and foundation. The base-isolated structure can be modeled as a viscously damped two degree of freedom system, and its generalized solution [18] is served as the baseline for the designing of isolation systems [19].

To optimize the governing parameters of the base isolator [20–22], H_2 [23,24] and H_∞ [25] optimization schemes are applauded [26]. H_∞ optimization technique is first proposed by Den Hartog [27] for evaluating the optimal system parameters for a dynamic vibration absorber [28–31] and the method is known as the fixed-point theory. Besides, H_2 optimization techniques are also exalted for random vibration [32,33] which was first proposed by Crandall and Mark [34]. The H_∞ optimization technique can only be implemented when the isolated structure is subjected to harmonic excitation [35].

Nowadays, the inerters induce inside or parallel to traditional base isolation (TBI) systems to enhance energy dissipation by amplifying the massive effective mass through rotational mass with motion transformers [36] inside the system. The inerter was first introduced by Smith [37] undermining the force to the current analogy for mitigation of vibration responses of the structures in 2002. Since then, these inerters have widely been implemented in mechanical systems as vibration control devices, especially for automobiles [38–43]. The inerters were often used in conjunction with other vibration control devices [44] to enhance its vibration reduction or energy dissipation performance [45–51]. For example, seismic performance [52,53] of a base-isolated building [54–58], water storage tank [59,60], are enhanced after coupling the inerters. Recently, Kuhnert et al. [61] critically reviewed the advantages and disadvantages of the inerter-based vibration isolation systems. The majority of the inerter based isolation devices are made of flywheel-gear inerter [54]. Apart from the fly-wheel based inerter, massive mass amplification can also be obtained by inertial amplifiers in which a large wide-bandgap can be achieved at low

* Corresponding author.
E-mail address: abanerjee@iitd.ac.in (A. Banerjee).

https://doi.org/10.1016/j.ijmecsci.2021.107044
Received 21 July 2021; Received in revised form 24 December 2021; Accepted 26 December 2021
Available online 15 January 2022

frequencies [62–65]. These characteristics of inertial amplifiers [66–70] allows to apply in structural member for vibration mitigation application [71–79]. Different types of negative stiffness devices like quasi-zero stiffness [80–83], high-static-low-dynamic stiffness [84,85], Euler buckled beams as negative stiffness elements [86–89], pseudo-negative-stiffness [90,91], negative-stiffness inclusions [92], magnetic negative stiffness dampers [93,94] are applied for the vibration isolation. In the field of metamaterial or periodic structures one type of negative stiffness arrangement has been reported which has a seemingly identical configuration with the inertial amplifiers [95–105]. However, the application of inertial amplifiers is minimal for complete structures, such as buildings [106] and bridges. As per the current literature review, most studies were based on structural members like beams and columns. However, they did not study any negative stiffness inertial amplifier-base-isolators. These could be the research gap of the study. Therefore, we have introduced the optimum negative stiffness inertial- amplifier-base-isolators for the single degree of freedom systems, an idealized version of a bridge, water tank, building or tower which have never been studied before in any existing literature. Additionally, the closed-form expressions for optimal design parameters have been introduced in this paper.

The H_2 and H_∞ optimization methods have been employed to derive these closed-form expressions for optimal design parameters such as frequency and viscous damping ratio of the novel isolators considering the random-white and harmonic base excitations, respectively. The optimal dynamic responses of each controlled structure have been obtained analytically. Using these results, each novel isolator's vibration reduction capacity (%) has been determined and compared to investigate their superior performance, respectively.

2. Structural model and equations of motion

The schematic diagram of a structure isolated by the NSIABI system subjected to harmonic and white-noise random excitation has been shown in Fig. 1(a). For the present study, the main structure has been considered as the single degree of freedom systems (SDOF), an idealized version of a bridge, water tank, building or tower. The free-body diagrams, along with the inertial forces, are shown in Fig. 1(c). Using these diagrams, the dynamic effective mass of the novel isolators have been derived. The other two isolators, namely, NSBI and IABI, have been achieved by categorizing the mass tuning ratio of NSIABI γ. The schematic diagrams of these isolators have been displayed in Fig. 1(d) and Fig. 1(e). These negative stiffness inertial amplifiers will enhance the energy dissipation capacity of the traditional base isolators, providing additional flexibility simultaneously sufficient load-bearing capacity to the controlled system. m_{ib}, k_{ib}, and c_{ib} are the base mass, stiffness, viscous damping of the novel isolators without the effect of negative stiffness devices and inertial amplifiers. After considering the effect of inertial amplifiers and negative stiffness devices, the dynamic effective mass, stiffness, and viscous damping of the novel isolators have been denoted as m_{ia}, k_{ia}, and c_{ia}, respectively. m_a refers to the mass of the inertial amplifier. m_1 and k_a are the mass and stiffness of the lateral spring–mass system, which has been attached to the top of the inertial amplifier's mass m_a. This lateral spring–mass system has behaved as a negative stiffness device that provides dynamic negative effective mass and stiffness to the novel isolators. $\ddot{u}_g$ defines the base excitation. These novel isolators have been installed at the base of the main structures. The system parameters of the main structures have been referred as mass m_s, stiffness k_s, and viscous damping c_s. Total static mass of the mass–spring–mass system at the lateral terminal of the inertial amplifier has been derived as $m_T = m_a + m_1$. Diving this equation by m_T and the individual masses have been expressed as

$$m_a = \gamma m_T \quad \text{and} \quad m_1 = (1-\gamma)m_T \tag{1}$$

The types of novel isolators that depends upon the value of γ have been listed below.

Table 1
The values of the mass tuning ratio of novel base isolation systems γ.

Mass tuning ratio	NSBI	NSIABI	IABI
γ	0	$0.1 < \gamma < 0.9$	1

Table 1 shows that for IABI, NSIABI, and NSBI systems, the tuning ratio for NSIABI of inertial amplifier γ is considered 1, $0 < \gamma < 1$, 0. $\ddot{u}_g$ defines the ground motions. The equations of motion of the lateral spring–mass systems in Fig. 1(b) are represented as

$$m_1\ddot{x}_1 + k_a(x_1 - x_a) = 0 \tag{2}$$

An inertial angle θ between the y-axis and rigid link is indicated in the diagrams when the inertial amplifier is undeformed. It is considered that the system moves towards the y-axis, and small deflections occurred in lateral masses m_a and m_1 in x and y-directions. x_a and y_a indicate the displacement of lateral masses in x and y-directions, respectively. The steady state solutions of the displacement responses under harmonic motions are evaluated as $x_a = X_a e^{i\omega t}$, $x_1 = X_1 e^{i\omega t}$. After substituting the values in Eq. (2), the values of x_1 are determined as

$$X_1 = \left(\frac{k_a}{k_a - \omega^2 m_1}\right) X_a \tag{3}$$

Now consider that the controlled system is in an equilibrium state. After balancing the momentum in x-direction, the frequency dependant effective mass has been derived as [102]

$$\begin{aligned} & m_{ae}\dot{x}_a = m_1\dot{x}_1 + m_a\dot{x}_a \\ \text{and} \quad & m_{ae} = (1-\gamma)m_T\left(\frac{k_a}{k_a - \omega^2 m_1}\right) + \gamma m_T \\ & = (1-\gamma)m_T\left(\frac{1}{1-\frac{\omega^2}{\omega_a^2}}\right) + \gamma m_T \end{aligned} \tag{4}$$

where m_{ae} defines the frequency dependent effective mass of the novel isolators. The natural frequency of the lateral spring–mass system/negative stiffness device has been derived $\omega_a = \sqrt{\frac{k_a}{m_1}}$, and the natural frequency of the main structure refers as $\omega_s = \sqrt{\frac{k_s}{m_s}}$. It is considered that the total system in Fig. 1(b) moves towards y-directions, and the displacement responses in x and y-directions of the lateral spring–mass systems attached at two terminals are evaluated as

$$y_a = \frac{y_1 + y_2}{2} \quad \text{and} \quad x_a = \pm\frac{y_2 - y_1}{2\tan\theta} \tag{5}$$

where y_a and x_a define the displacement of frequency dependent lateral mass in y and x-directions, respectively. The inertial forces developed through the lateral spring–mass systems are derived as

$$f_{ix} = m_{ae}\ddot{x}_a \quad \text{and} \quad f_{iy} = m_{ae}\ddot{y}_a \tag{6}$$

where f_{ix} and f_{iy} refer the inertial forces in x and y-direction, respectively. The internal forces through the rigid links are obtained as f_1 and f_2 and presented in Fig. 1(c). The values of f_1 and f_2 have been derived as

$$f_1 = \frac{1}{2}\left(\frac{f_{ix}}{\sin\theta} - \frac{f_{iy}}{\cos\theta}\right) \quad \text{and} \quad f_2 = \frac{1}{2}\left(\frac{f_{ix}}{\sin\theta} + \frac{f_{iy}}{\cos\theta}\right) \tag{7}$$

The total reaction forces developed through the links are presented in Fig. 1(c) and evaluated as

$$F = -2f_1\cos\theta + k_{ib}(y_2 - y_1) = d_1\left(\ddot{y}_2 - \ddot{y}_1\right) + d_2\left(\ddot{y}_2 + \ddot{y}_1\right) + k_{ia}(y_2 - y_1) \tag{8}$$

where $d_1 = \left(0.5m_{ae}/\tan^2\theta\right)$ and $d_2 = 0.5m_{ae}$ are the constants produced through the balancing of the inertial forces generated in the inertial amplifier which is presented in Fig. 1(a). In the lateral masses, the total inertial forces are proportional to the mean of accelerations $\left(\frac{\ddot{y}_2 + \ddot{y}_1}{2}\right)$

generated through the two terminals of the inertial amplifier and the inertial constant d_2 is produced through that. d_1 constant produced by the inertial forces generated in the geometry of the inertial amplifier and the lateral masses of the entire system. It is observed that the inertial forces of the entire system is directly proportional to the relative acceleration $\left(\frac{\ddot{y}_2-\ddot{y}_1}{2}\right)$ between two terminals. After considering inertial constants, d_1 and d_2, the total dynamic effective masses of the novel isolators have been derived as

$$\begin{aligned} m_{ia} &= m_{ib} + 0.5m_{ae}\left(1+\frac{1}{\tan^2\theta}\right) \\ &= m_{ib} + \Theta\left((1-\gamma)m_T\left(\frac{\omega_a^2}{\omega_a^2-\omega^2}\right)+\gamma m_T\right) \end{aligned} \tag{9}$$

where $\Theta = 0.5\left(1+\frac{1}{\tan^2\theta}\right)$. Simultaneously, using Eq. (9), the total dynamic effective stiffness of the novel isolators have been derived and expressed as

$$k_{ia} = m_{ia}\omega_{ib}^2 = \frac{\omega_{ib}^2{\omega_a}^2 m_\vartheta - \omega_{ib}^2\omega^2 m_{\boldsymbol{\Phi}}}{{\omega_a}^2-\omega^2} \tag{10}$$

where $m_{\boldsymbol{\Phi}} = (\Theta m_T\gamma + m_{ib})$ and $m_\vartheta = (\Theta m_T + m_{ib})$. In Eq. (10), k_{ib} contains the dynamic negative stiffness and presented as $(-\omega_{ib}^2\omega^2 m_{\boldsymbol{\Phi}})$. The generalized equations of motion of the structures isolated by the novel isolators have been derived as

$$\begin{aligned} m_{ia}\ddot{y}_{ib} + c_{ia}\dot{y}_{ib} + k_{ia}y_{ib} - k_s y_s - c_s\dot{y}_s &= -m_{ia}\ddot{u}_g \\ m_s\ddot{y}_s + c_s\dot{y}_s + k_s y_s &= -m_s(\ddot{u}_g + \ddot{y}_{ib}) \end{aligned} \tag{11}$$

The ratio of the excitation frequency to the natural frequency of the main structure has been defined as $\eta = \frac{\omega}{\omega_s}$, the ratio of the total effective mass of the novel isolators to the main structure refer as $\mu_{ia} = \frac{m_{ia}}{m_s}$, the frequency ratio of the novel isolators to the main structure denote as $\eta_{ib} = \frac{\omega_{ib}}{\omega_s}$, the viscous damping ratio of the novel isolators denote as $\zeta_{ib} = \frac{c_{ia}}{2m_{ia}\omega_{ib}}$, and the damping ratio of the main structure is define as $\zeta_s = \frac{c_s}{2m_s\omega_s}$, the natural frequency of the novel isolators denote as $\omega_{ib} = \sqrt{\frac{k_{ia}}{m_{ia}}}$. The total static mass of the novel isolators has been derived as $m_{ib}+2m_T$. From Eq. (11), inertial amplifications need to be determined and are evaluated as

$$\alpha = \frac{m_T}{m_{ib}+2m_T} \quad \text{and} \quad m_T = \left(\frac{\alpha}{1-2\alpha}\right)m_{ib} \tag{12}$$

In Eq. (12), α defines the ratio of total lateral mass to total static mass of the novel isolators.

$$\beta = \frac{m_{ib}}{m_{ib}+2m_T} = (1-2\alpha) \tag{13}$$

In Eq. (13), β defines the ratio of base mass to total static mass of the novel isolators.

$$\begin{aligned} m_f &= \frac{m_{ib}}{m_{ib}+2m_T} + \frac{m_T}{m_{ib}+2m_T}\Theta\left((1-\gamma)\left(\frac{\omega_a^2}{\omega_a^2-\omega^2}\right)+\gamma\right) \\ &= (1-2\alpha) + \alpha\Theta\left((1-\gamma)\left(\frac{1}{1-\frac{\eta^2}{\eta_a^2}}\right)+\gamma\right) \end{aligned} \tag{14}$$

For static condition, it is considered that the value of $\eta/\eta_a = 0$. Now, the closed-form expression for the static effective mass m_{fs} has been derived as

$$m_{fs} = (1-2\alpha) + \alpha\Theta \tag{15}$$

where $\Theta = 0.5\left(1+\frac{1}{\tan^2\theta}\right)$. In Eq. (14), m_f refers the dynamic effective mass ratio of the total frequency dependent effective mass m_{ia} to total static mass of the novel isolators $(m_{ib}+2m_T)$. Where $\eta = \omega/\omega_s$ which defines the ratio of the excitation frequency to the natural frequency of the main structure and $\eta_a = \omega_a/\omega_s$ which defines the ratio of the frequency of lateral spring–mass system to the main structure, respectively. The effect of negative stiffness and inertial amplifier on the static mass of the novel isolators need to be investigated. To perform that contour plot of Eq. (14) and Eq. (15) have been displayed in Fig. 2. Precisely, Fig. 2(a) shows the contour of the static effective mass ratio (m_{fs}) as a function of the ratio of total lateral mass to the total static mass and inertial angle of novel isolators. It shows that the effective mass amplification occurred at $\theta \le 30°$, which have been recognized as the critical angles for the novel isolators, respectively. Besides, the significant amount of mass amplification occurred at $\theta \le 12°$. Therefore, $\theta \le 12°$ have been applied throughout the paper for determining the results, respectively. Interestingly, the presence of negative effective mass has not been observed in Fig. 2(a), but it has been observed in Fig. 2(b) where $\eta/\eta_a \ne 0$. Fig. 2(b) shows the contour of the dynamic effective mass ratio (m_f) as a function of mass tuning ratio and frequency ratio of inertial amplifier. Most of the dynamic negative effective mass has been observed at $1.01 \le \eta/\eta_a \le 1.84$ and $\gamma = 0$ (NSBI), which indicates that the installed lateral spring–mass system at two terminals of the inertial amplifier has behaved as a negative stiffness device. Another observation is that the presence of effective negative mass decreases when the mass tuning ratio increases. The frequency region of dynamic negative effective mass also decreases when the mass tuning ratio increases. For $0.1 \le \gamma \le 0.5$ (NSIABI), the region of negative effective mass is the most, whereas the negative effective mass region shortened at $0.6 \le \gamma \le 0.9$ (NSIABI). Precisely, the negative effective mass has become zero when $\gamma = 1$ (IABI) where the mass of the negative stiffness device m_1 is zero and simultaneously, the corresponding value of the stiffness becomes zero. The dynamic effective mass of the novel isolators has been amplified at $\eta > 1.84$, and a significant amount of mass amplification occurs at $\gamma = 1$ (IABI). Overall, NSBI ($\gamma = 0$) and NSIABI ($0.1 \le \gamma \le 0.5$) produce a significant amount of negative effective mass amplification. In contrast, a significant amount of positive effective mass amplification has been observed in IABI ($\gamma = 1$) and other NSIABI systems having the values of $0.6 \le \gamma \le 0.9$. Therefore, the dynamic effective mass becomes negative for frequencies near the inertial amplifier's resonance frequency, respectively. This negative effective mass has been effected the dynamic stiffness of the isolators.

Now, the change of dynamic effective stiffness concerning the total static stiffness has been investigated. To perform that, the dynamic effective stiffness ratio k_f has been introduced, which is defined as the ratio of total dynamic effective stiffness to the static stiffness of the novel isolators, respectively. Therefore, the mathematical expression of the k_f has been derived as

$$k_f = \frac{k_{ia}}{k_{ib}} = \frac{\omega_{ib}^2{\omega_a}^2 m_\vartheta - \omega_{ib}^2\omega^2 m_{\boldsymbol{\Phi}}}{\left(m_{ib}\omega_{ib}^2\right)\left({\omega_a}^2-\omega^2\right)} = \frac{{\omega_a}^2 m_\vartheta - \omega^2 m_{\boldsymbol{\Phi}}}{m_{ib}\left({\omega_a}^2-\omega^2\right)} \tag{16}$$

Now, the numerator and denominator of Eq. (16) has been divided by $m_s\omega_s^2$ to transform it into non-dimensional form. Therefore, the non-dimensional form of Eq. (16) has been derived as

$$k_f = \frac{\eta_{ib}^2{\eta_a}^2\mu_\vartheta - \eta_{ib}^2\eta^2\mu_{\boldsymbol{\Phi}}}{\left(\mu_{ib}\eta_{ib}^2\right)\left({\eta_a}^2-\eta^2\right)} = \frac{\Theta\left(\frac{\mu_T}{\mu_{ib}}\right)+1-\left(\frac{\eta^2}{\eta_a^2}\right)\Theta\left(\frac{\mu_T}{\mu_{ib}}\right)\gamma-\left(\frac{\eta^2}{\eta_a^2}\right)}{\left(1-\left(\frac{\eta^2}{\eta_a^2}\right)\right)} \tag{17}$$

where $\mu_{\boldsymbol{\Phi}} = m_{\boldsymbol{\Phi}}/m_s = (\Theta\mu_T\gamma + \mu_{ib})$, $\mu_\vartheta = m_\vartheta/m_s = (\Theta\mu_T + \mu_{ib})$, and $\mu_T = m_T/m_s$. The governing parameters are μ_{ib}, γ, θ, and μ_T. For static effective stiffness condition, at $\eta/\eta_a = 0$, the closed-form expression for the static effective stiffness k_{fs} has been derived as

$$k_{fs} = 0.5\left(1+\frac{1}{\tan^2\theta}\right)\left(\frac{\mu_T}{\mu_{ib}}\right)+1 \tag{18}$$

The effect of negative stiffness devices and inertial amplifiers on the static effective stiffness of the novel isolators also needs to be investigated. To perform that contour plot of Eq. (18) as a function of the ratio of total lateral mass ratio to base mass ratio and inertial angle has been displayed in Fig. 3(a), respectively. The presence of negative effective mass has not been observed in these figures. Instead of that, the effective stiffness of the novel isolators amplifies. At higher

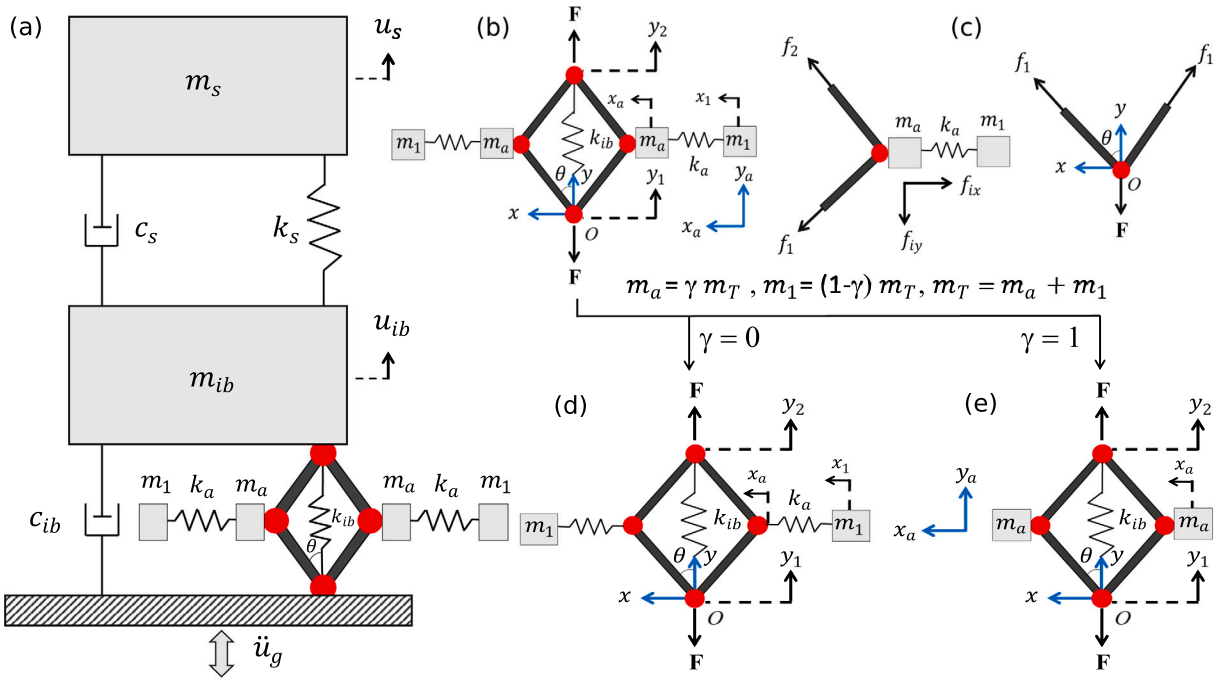

Fig. 1. (a) The generalized theoretical model of a dynamic system isolated by negative stiffness inertial amplifier base isolator, (b) negative stiffness based inertial amplifier base isolator, (c) free-body diagrams of NSIABI, (d) negative stiffness based isolator, and (e) inertial amplifier base isolator.

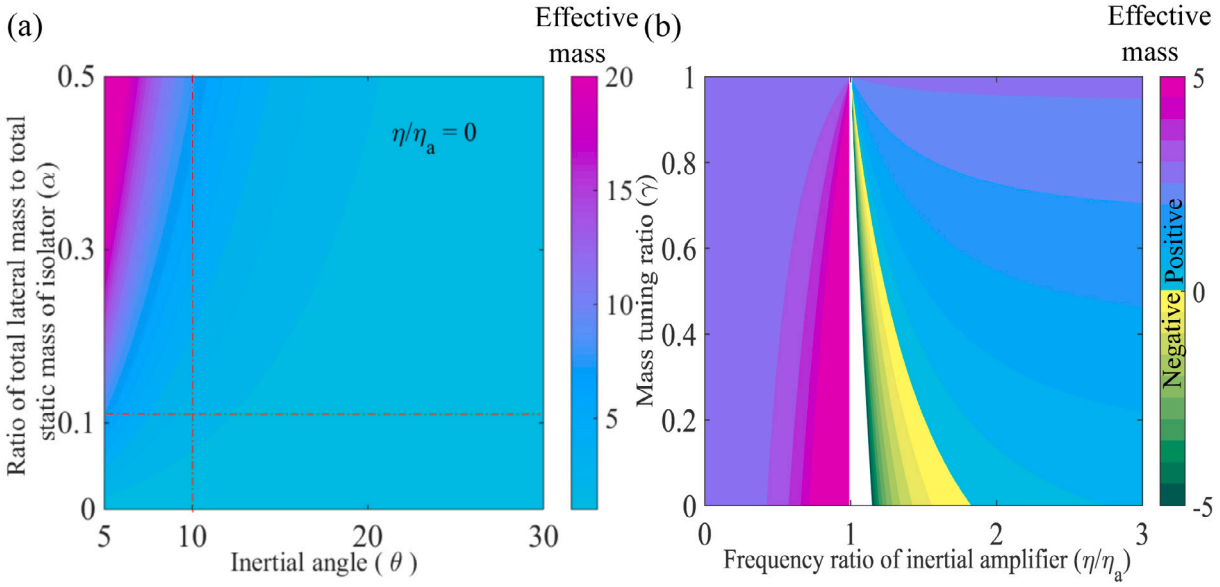

Fig. 2. (a) The contour plot of the static effective mass ratio (m_{fs}) as a function of the ratio of total lateral mass to the total static mass of isolator α and inertial angle θ has been drawn, where the value of frequency ratio of the inertial amplifier η/η_a is considered as 0. From this plot, $\alpha = 0.11$ and $\theta = 10°$ have been taken to draw the graph for the dynamic effective mass ratio (m_f). These points have been indicated by red dash-dotted vertical and horizontal lines. (b) Using these values, the contour plot of dynamic effective mass ratio (m_f) as a function of mass tuning ratio γ and frequency ratio of the inertial amplifier η/η_a has been drawn. The dynamic effective mass becomes negative for frequencies near the inertial amplifier's resonance frequency.

inertial angle (i.e., $12° < \theta \leq 30°$), the inertial force decreases while the inertial forces increases at lower angle (i.e., $\theta \leq 12°$). Therefore, the negative effective stiffness is a dynamic characteristic of these novel isolators, which can only be achieved when the excitation frequency ratio (η) is present. The effect of negative stiffness devices and inertial amplifiers on the dynamic effective stiffness of the novel isolators has been investigated. To perform that, the contour plot of Eq. (17) as a function of mass tuning ratio, the frequency ratio of the inertial amplifier has been displayed in Fig. 3(b). The values of the dynamic effective stiffness of the novel isolators increases the mass tuning ratio decreases for frequency region $0.65 \leq \eta/\eta_a \leq 1.0$ and the significant amount of drop has occurred at $1.01 \leq \eta/\eta_a \leq 1.84$ where most of the contour region is full of negative effective stiffness. Another observation is that the presence of effective negative stiffness decreases when the mass tuning ratio increases. Simultaneously, the frequency region of dynamic negative effective stiffness also decreases when the mass tuning ratio increases. For $0.1 \leq \gamma \leq 0.5$ (NSIABI), the region of negative effective stiffness is the most, whereas the negative effective stiffness region shortened at $0.6 \leq \gamma \leq 0.9$ (NSIABI). Precisely, the negative effective stiffness has become zero when $\gamma = 1$ (IABI) where

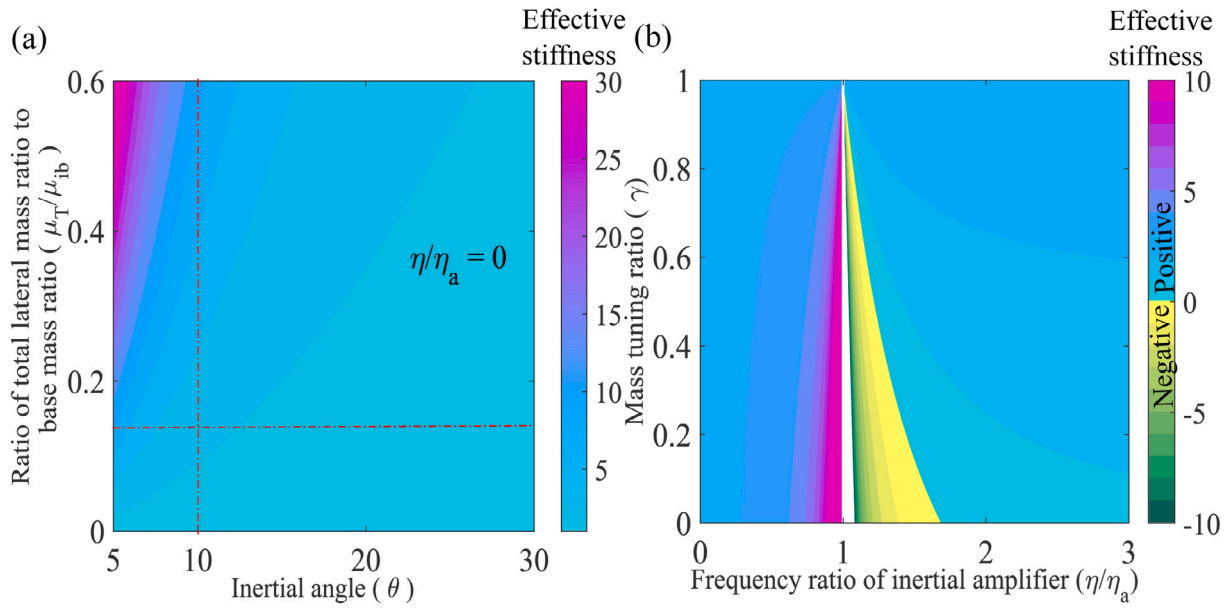

Fig. 3. (a) The contour plot of the static effective stiffness ratio (k_{fs}) as a function of the ratio of total lateral mass ratio to base mass ratio μ_T/μ_{ib} and inertial angle θ has been drawn, where the value of frequency ratio of the inertial amplifier η/η_a is considered as 0. From this plot, $\mu_T/\mu_{ib} = 0.14$ and $\theta = 10°$ have been taken to plot the graphs for dynamic effective stiffness ratio (k_f). These points have been indicated by red dash-dotted vertical and horizontal lines. (b) Using these values, the contour plot of the dynamic effective stiffness ratio (k_f) as a function of mass tuning ratio γ and frequency ratio of the inertial amplifier η/η_a has been drawn. The dynamic effective stiffness becomes negative for frequencies near the inertial amplifier's resonance frequency.

the mass of the negative stiffness device m_1 is zero and simultaneously, the corresponding value of the stiffness becomes zero. The dynamic effective stiffness of the novel isolators has been amplified at $\eta > 1.84$, and most of the stiffness amplification occurs at $\gamma = 1$ (IABI). Overall, NSBI ($\gamma = 0$) and NSIABI ($0.1 \le \gamma \le 0.5$) produce a significant amount of dynamic negative effective stiffness amplification, providing additional flexibility extends the time period of the isolators, respectively. Hence, The base displacement of the isolator will be more in that particular region, which helps to increase the vibration reduction capacity of NSBI and NSIABI, respectively. In contrast, a significant amount of positive dynamic effective stiffness amplification has been observed in IABI ($\gamma = 1$) and other NSIABI systems having the values of $0.6 \le \gamma \le 0.9$. Additionally, the dynamic effective stiffness amplifications at $0.65 \le \eta/\eta_a \le 1.0$ and $2 \le \eta/\eta_a \le 3.0$ provides sufficient load-bearing capacity to the controlled structures during vibration simultaneously. These unique dynamic properties of the novel isolators provide more resistance than the traditional base isolator to the controlled structures against vibrations. Finally, it has been summarized that these negative stiffness inertial amplifiers based isolators have enhanced the energy dissipation capacity of the traditional base isolators, providing additional flexibility simultaneously sufficient load-bearing capacity to the controlled structures, respectively.

In Eq. (11), the relative displacement of main structure and novel isolators has been derived as $y_s = (u_s - u_{ib})$ and $y_{ib} = (u_{ib} - u_g)$. Now considers that this isolated structure is subjected to harmonic ground motions, respectively. Therefore, the steady state solutions are considered as $y_s = Y_s e^{i\omega t}$, $y_{ib} = Y_{ib} e^{i\omega t}$, and $\ddot{u}_g = U_g e^{i\omega t}$. Here, $(\dot{\bullet})$ defines the derivative with respect to time. By substituting these steady state solutions in Eq. (11), a transfer matrix has been formed. Using this matrix, the displacement responses of the main structure and NSIABI system have been derived analytically. Therefore, the matrix has been derived as

$$\begin{bmatrix} 2q\zeta_s\omega_s + q^2 + \omega_s{}^2 & q^2 \\ -2q\zeta_s\omega_s - \omega_s{}^2 & \frac{(2q\zeta_{ib}\omega_{ib}+q^2+\omega_{ib}{}^2)(q^2\mu_\Phi+\omega_a{}^2\mu_\vartheta)}{q^2+\omega_a{}^2} \end{bmatrix} \begin{Bmatrix} Y_s \\ Y_{ib} \end{Bmatrix} = -\begin{bmatrix} 1 \\ \mu_{ia} \end{bmatrix} U_g \tag{19}$$

where $q = i\omega$, $\mu_{ia} = \mu_{ib} + \frac{\Theta\,\mu_T(\gamma\,q^2+\omega_a{}^2)}{q^2+\omega_a{}^2}$ or $\mu_{ia} = \frac{q^2\mu_\Phi+\omega_a{}^2\mu_\vartheta}{q^2+\omega_a{}^2}$, and $\Theta = 0.5\left(1 + \frac{1}{\tan^2\theta}\right)$. μ_{ib} defines the ratio of base mass to the structural mass of the isolated structures (i.e., $\mu_{ib} = m_{ib}/m_s$). Transfer matrix is a matrix approach to derive the responses of the dynamic systems in the frequency domain. Using Eq. (19), the transfer functions of displacement responses of main structure H_s and NSIABI system H_{ib} have been obtained analytically. Therefore, the displacement response of the main structure has been derived as

$$H_s(i\omega) = \frac{Y_s}{U_g} = \frac{-\left(q^2\mu_\Phi + \omega_a{}^2\mu_\vartheta\right)\omega_{ib}\left(2q\zeta_{ib} + \omega_{ib}\right)}{\Delta_n} \tag{20}$$

The displacement response of the novel isolators have been derived as

$$H_{ib}(i\omega) = \frac{Y_{ib}}{U_g} = \frac{\begin{pmatrix} -2\zeta_s\mu_\Phi\omega_s q^3 - 2\zeta_s\mu_\vartheta\omega_a{}^2\omega_s q - \mu_\Phi q^4 - 2q^3\zeta_s\omega_s \\ -q^2\mu_\Phi\omega_s{}^2 - q^2\mu_\vartheta\omega_a{}^2 - 2q\zeta_s\omega_a{}^2\omega_s \\ -\mu_\vartheta\omega_a{}^2\omega_s{}^2 - q^2\omega_s{}^2 - \omega_a{}^2\omega_s{}^2 \end{pmatrix}}{\Delta_n} \tag{21}$$

where the closed-form expression for Δ_n has been derived as

$$\begin{aligned} \Delta_n(i\omega) = {} & q^6\mu_\Phi + \left(2\,\mu_\Phi\omega_{ib}\zeta_{ib} + 2\,\zeta_s\mu_\Phi\omega_s + 2\,\zeta_s\omega_s\right)q^5 \\ & + \left(4\,\zeta_s\mu_\Phi\zeta_{ib}\omega_s\omega_{ib} + \mu_\Phi\omega_{ib}{}^2 + \mu_\Phi\omega_s{}^2 + \mu_\vartheta\omega_a{}^2 + \omega_s{}^2\right)q^4 \\ & + \begin{pmatrix} 2\,\mu_\Phi\omega_{ib}\zeta_{ib}\omega_s{}^2 + 2\,\zeta_{ib}\omega_a{}^2\omega_{ib}\mu_\vartheta \\ +2\,\zeta_s\mu_\Phi\omega_{ib}{}^2\omega_s + 2\,\zeta_s\mu_\vartheta\omega_a{}^2\omega_s + 2\,\zeta_s\omega_a{}^2\omega_s \end{pmatrix}q^3 \\ & + \begin{pmatrix} 4\,\zeta_s\zeta_{ib}\omega_a{}^2\omega_s\omega_{ib}\mu_\vartheta + \mu_\Phi\omega_{ib}{}^2\omega_s{}^2 \\ +\mu_\vartheta\omega_a{}^2\omega_{ib}{}^2 + \mu_\vartheta\omega_a{}^2\omega_s{}^2 + \omega_a{}^2\omega_s{}^2 \end{pmatrix}q^2 \\ & + \left(2\,\zeta_{ib}\mu_\vartheta\omega_a{}^2\omega_{ib}\omega_s{}^2 + 2\,\zeta_s\mu_\vartheta\omega_a{}^2\omega_{ib}{}^2\omega_s\right)q \\ & + \mu_\vartheta\omega_a{}^2\omega_{ib}{}^2\omega_s{}^2 \end{aligned} \tag{22}$$

The shear force of the isolated structure has been derived as

$$H_{sf}(i\omega) = \frac{q\zeta_s Y_s + \omega_s^2 Y_s}{U_g} = \frac{\begin{pmatrix} -\left(q^2\mu_\Phi + \omega_a{}^2\mu_\vartheta\right) \\ \omega_{ib}\left(2q\zeta_{ib} + \omega_{ib}\right) \end{pmatrix}\left(q\zeta_s + \omega_s{}^2\right)}{\Delta_n} \tag{23}$$

Before obtaining the dynamic responses of isolated structures, the optimal values of design parameters need to be determined. Therefore, H_2 and H_∞ optimization methods have been employed to obtain these optimal design parameters, respectively. The basic principle of H_∞

optimization method is to minimize the maximum amplitude of the frequency response based on the fixed-point theory, [27] and this optimization method is only applicable when the controlled structures are subjected to harmonic excitations, respectively. Where the H_2 optimization method targets to minimize the mean squared displacement of the main structure under random excitation, respectively. The evaluation procedures of both are entirely different, and the detailed process has been illustrated below.

3. H_2 Optimization for white-noise random excitation

H_2 optimization has been performed to minimize the total energy of these dynamic systems above all frequencies. Thus, when these controlled systems are subjected to white-noise random excitations instead of harmonic excitations, the H_2 norm is more effective than H_∞. Therefore, the closed-form expressions for optimal design parameters of the novel isolators have been derived using this optimization method. To perform this study, Eq. (11) has been written in a generalized form which is expressed as

$$\mathbf{M}\ddot{\mathbf{y}}(t) + \mathbf{C}\dot{\mathbf{y}}(t) + \mathbf{K}\mathbf{y}(t) = -\mathbf{M}\mathbf{r}\ddot{\mathbf{u}}_g(t) \tag{24}$$

where $r = [1, 1]^T$ and $\ddot{\mathbf{u}}_g(t)$ defines as the forcing vector. Each force acts to the corresponding degree of freedom. The general form of the forcing function is represented as

$$\ddot{\mathbf{u}}_g(t) = \begin{Bmatrix} \ddot{u}_{g1}(t) \\ \ddot{u}_{g2}(t) \\ \cdots \\ \ddot{u}_{gn}(t) \end{Bmatrix} \tag{25}$$

Each component of force $\ddot{u}_{g_j}(t)$ is randomly correlated, where $j = 1, 2, 3 \cdots n$. The power spectral density matrix is formed as

$$\mathbf{S}_{U_g U_g}(\omega) = E[\mathbf{U}_g(\omega)^* \mathbf{U}_g(\omega)] = \begin{bmatrix} S_{U_{g1}U_{g1}}(\omega) & S_{U_{g1}U_{g2}}(\omega) & \cdots & S_{U_{g1}U_{gn}}(\omega) \\ S_{U_{g2}U_{g1}}(\omega) & S_{U_{g2}U_{g2}}(\omega) & \cdots & S_{U_{g2}U_{gn}}(\omega) \\ \cdots & \cdots & \cdots & \cdots \\ S_{U_{gn}U_{g1}}(\omega) & S_{U_{gn}U_{g2}}(\omega) & \cdots & S_{U_{gn}U_{gn}}(\omega) \end{bmatrix} \tag{26}$$

$(\bullet)^*$ denotes complex conjugate. In Eq. (26), the off-diagonal values are indicated as cross power spectral density functions and the diagonal values are indicated as auto power spectral density functions. The steady solutions are expressed as $\ddot{\mathbf{u}}_g(t) = \mathbf{U}_g(\omega)e^{i\omega t}$ and $\mathbf{y}(t) = \mathbf{Y}(\omega)e^{i\omega t}$. Now, substituting these values in Eq. (24) to obtain frequency-domain expressions. Therefore, the frequency-domain expressions are expressed as

$$\begin{aligned} &(q^2\mathbf{M} + q\mathbf{C} + \mathbf{K})\mathbf{Y}(\omega) = -\mathbf{M}\mathbf{r}\mathbf{U}_g(\omega), \\ &\mathbf{U}(\omega)\mathbf{Y}(\omega) = -\mathbf{M}\mathbf{r}\mathbf{U}_g(\omega) \quad \text{and} \quad \mathbf{Y}(\omega) = \mathbf{H}(\omega)\mathbf{U}_g(\omega) \end{aligned} \tag{27}$$

where $q = \mathrm{i}\omega$. Now, the power spectral density matrix of displacement responses which contains $\mathbf{y}(t)$ has been formed and expressed as

$$\mathbf{S}_{YY}(\omega) = E[\mathbf{Y}(\omega)\mathbf{Y}^*(\omega)] = \mathbf{H}(\omega)\mathbf{S}_{U_g U_g}(\omega)\mathbf{H}^*(\omega) \tag{28}$$

where $(\bullet)^*$ refers the complex conjugate transpose. Hence, the standard deviation of the displacement of the main structure has been derived using Eq. (28) and solved by the formula below.

$$\sigma_{y_s}^2 = E[y_s^2(t)] = \int_{-\infty}^{\infty} |H_s(\omega)|^2 S_{U_g U_g}(\omega)\, \mathrm{d}\omega \tag{29}$$

Now, the velocity of the main structure has been determined as

$$\dot{Y}_s(\omega) = (\mathrm{i}\omega)Y_s(\omega) = (\mathrm{i}\omega)H_s(\omega)U_g(\omega) \tag{30}$$

Considering the above equation, the standard deviation for the velocity of the main structure is obtained as

$$\sigma_{\dot{y}_s}^2 = E[\dot{y}_s^2(t)] = \int_{-\infty}^{\infty} \omega^2 |H_s(\omega)|^2 S_{U_g U_g}(\omega)\mathrm{d}\omega \tag{31}$$

The calculation of the integral on the right-hand side of equations Eq. (29) and Eq. (31) in general requires the calculation of integrals involving the ratio of polynomials of the following form.

$$I_n = \int_{-\infty}^{\infty} \frac{\Xi_n(\omega)\, \mathrm{d}\omega}{\Lambda_n(\mathrm{i}\omega)\Lambda_n^*(\mathrm{i}\omega)} \tag{32}$$

Here the polynomials are expressed as

$$\Xi_n(\omega) = b_{n-1}\omega^{2n-2} + b_{n-2}\omega^{2n-4} + \cdots + b_0 \tag{33}$$

$$\Lambda_n(\mathrm{i}\omega) = a_n(\mathrm{i}\omega)^n + a_{n-1}(\mathrm{i}\omega)^{n-1} + \cdots + a_0 \tag{34}$$

Following Roberts and Spanos, [107] this integral is expressed as

$$I_n = \frac{\pi}{a_n} \frac{\det[\mathbf{N}_n]}{\det[\mathbf{D}_n]} \tag{35}$$

Here the $n \times n$ matrices are defined as

$$\mathbf{N}_n = \begin{bmatrix} b_{n-1} & b_{n-2} & & \cdots & & & b_0 \\ -a_n & a_{n-2} & -a_{n-4} & a_{n-6} & \cdots & 0 & \cdots \\ 0 & -a_{n-1} & a_{n-3} & -a_{n-5} & \cdots & 0 & \cdots \\ 0 & a_n & -a_{n-2} & a_{n-4} & \cdots & 0 & \cdots \\ 0 & \cdots & & & \cdots & 0 & \cdots \\ 0 & 0 & & & \cdots & -a_2 & a_0 \end{bmatrix} \tag{36}$$

and

$$\mathbf{D}_n = \begin{bmatrix} a_{n-1} & -a_{n-3} & a_{n-5} & -a_{n-7} & & & \\ -a_n & a_{n-2} & -a_{n-4} & a_{n-6} & \cdots & 0 & \cdots \\ 0 & -a_{n-1} & a_{n-3} & -a_{n-5} & \cdots & 0 & \cdots \\ 0 & a_n & -a_{n-2} & a_{n-4} & \cdots & 0 & \cdots \\ 0 & \cdots & & & \cdots & 0 & \cdots \\ 0 & 0 & & & \cdots & -a_2 & a_0 \end{bmatrix} \tag{37}$$

As the random excitation is considered Gaussian white noise with zero mean and standard deviation two, its spectral density is constant for all frequencies. But different spectral densities can also easily be used within the scope of this formulation. Hence, we have considered that the forcing function has constant spectral density. So, we assume that

$$S_{U_g U_g}(\omega) = S_0 \tag{38}$$

As mentioned before that the input spectrum is considered as white-noise random excitation. Thus S_0 refers to constant for all frequencies. Therefore, using Eq. (29), the standard deviation of displacement response of main structure $y_s(t)$ has been obtained as

$$\sigma_{y_s}^2 = \int_{-\infty}^{\infty} |H_s(\omega)|^2 S_0\, \mathrm{d}\omega = S_0 \int_{-\infty}^{\infty} \frac{\Xi_n(\omega)}{\Delta_n(\mathrm{i}\omega)\Delta_n^*(\mathrm{i}\omega)}\, \mathrm{d}\omega \tag{39}$$

Now, using Eq. (31), The standard deviation of the velocity of the main structure has been derived as

$$\sigma_{\dot{y}_s}^2 = \int_{-\infty}^{\infty} \omega^2 |H_s(\omega)|^2 S_0\, \mathrm{d}\omega = S_0 \int_{-\infty}^{\infty} \frac{\omega^2 \Xi_n(\omega)}{\Delta_n(\mathrm{i}\omega)\Delta_n^*(\mathrm{i}\omega)}\, \mathrm{d}\omega \tag{40}$$

Finally, The standard deviation of shear force of these isolated structures have been derived as

$$\sigma_{sf}^2 = \int_{-\infty}^{\infty} |H_{sf}(\omega)|^2 S_0\, \mathrm{d}\omega \tag{41}$$

It is considered that the proposed negative stiffness inertial-amplifier-base-isolators are subjected to Gaussian White Noise, and the root means square responses of the main systems are evaluated from Eq. (11). The determinant of the solution is obtained from the matrix

form of Eq. (19) as

$$\Delta_n(\mathrm{i}\omega) = \begin{array}{c} q^6\mu_{\boldsymbol{\Phi}} + \left(2\,\mu_{\boldsymbol{\Phi}}\omega_{ib}\zeta_{ib} + 2\,\zeta_s\mu_{\boldsymbol{\Phi}}\omega_s + 2\,\zeta_s\omega_s\right) q^5 \\ + \left(4\,\zeta_s\mu_{\boldsymbol{\Phi}}\zeta_{ib}\omega_s\omega_{ib} + \mu_{\boldsymbol{\Phi}}{\omega_{ib}}^2 + \mu_{\boldsymbol{\Phi}}{\omega_s}^2 + \mu_\vartheta{\omega_a}^2 + {\omega_s}^2\right) q^4 \\ + \begin{pmatrix} 2\,\mu_{\boldsymbol{\Phi}}\omega_{ib}\zeta_{ib}{\omega_s}^2 + 2\,\zeta_{ib}{\omega_a}^2\omega_{ib}\mu_\vartheta \\ +2\,\zeta_s\mu_{\boldsymbol{\Phi}}{\omega_{ib}}^2\omega_s + 2\,\zeta_s\mu_\vartheta{\omega_a}^2\omega_s + 2\,\zeta_s{\omega_a}^2\omega_s \end{pmatrix} q^3 \\ + \begin{pmatrix} 4\,\zeta_s\zeta_{ib}{\omega_a}^2\omega_s\omega_{ib}\mu_\vartheta + \mu_{\boldsymbol{\Phi}}{\omega_{ib}}^2{\omega_s}^2 \\ +\mu_\vartheta{\omega_a}^2{\omega_{ib}}^2 + \mu_\vartheta{\omega_a}^2{\omega_s}^2 + {\omega_a}^2{\omega_s}^2 \end{pmatrix} q^2 \\ + \left(2\,\zeta_{ib}\mu_\vartheta{\omega_a}^2\omega_{ib}{\omega_s}^2 + 2\,\zeta_s\mu_\vartheta{\omega_a}^2{\omega_{ib}}^2\omega_s\right) q \\ +\mu_\vartheta{\omega_a}^2{\omega_{ib}}^2{\omega_s}^2 \end{array} \tag{42}$$

It is observed that Eq. (42) is a 6th order polynomial equation. The standard deviation values for the displacement, velocity, and shear force of the structure isolated by the novel isolators have been determined using Eq. (32), the integral form has been derived as

$$\int_{-\infty}^{\infty}\frac{\Xi_n(\omega)}{\Delta_n(\mathrm{i}\omega)\Delta_n^*(\mathrm{i}\omega)}\mathrm{d}\omega = \frac{\pi}{a_6}\frac{\det\begin{bmatrix} b_5 & b_4 & b_3 & b_2 & b_1 & b_0 \\ -a_6 & a_4 & -a_2 & a_0 & 0 & 0 \\ 0 & -a_5 & a_3 & -a_1 & 0 & 0 \\ 0 & a_6 & -a_4 & a_2 & -a_0 & 0 \\ 0 & 0 & a_5 & -a_3 & a_1 & 0 \\ 0 & 0 & -a_6 & a_4 & -a_2 & a_0 \end{bmatrix}}{\det\begin{bmatrix} a_5 & -a_3 & a_1 & 0 & 0 & 0 \\ -a_6 & a_4 & -a_2 & a_0 & 0 & 0 \\ 0 & -a_5 & a_3 & -a_1 & 0 & 0 \\ 0 & a_6 & -a_4 & a_2 & -a_0 & 0 \\ 0 & 0 & a_5 & -a_3 & a_1 & 0 \\ 0 & 0 & -a_6 & a_4 & -a_2 & a_0 \end{bmatrix}} \tag{43}$$

The values of a_n and b_n have been listed in Appendix A, where $n = 1, 2, \ldots, 6$. After considering $\zeta_s = 0$, the determinant is represented as

$$\Delta_n(\mathrm{i}\omega) = \begin{pmatrix} q^6\mu_{\boldsymbol{\Phi}} + 2\,q^5\zeta_{ib}\mu_{\boldsymbol{\Phi}}\omega_{ib} \\ + \left(\mu_{\boldsymbol{\Phi}}{\omega_{ib}}^2 + \mu_{\boldsymbol{\Phi}}{\omega_s}^2 + {\omega_a}^2\mu_\vartheta + {\omega_s}^2\right) q^4 \\ +2\,\zeta_{ib}\omega_{ib}\left(\mu_{\boldsymbol{\Phi}}{\omega_s}^2 + {\omega_a}^2\mu_\vartheta\right) q^3 \\ + \left(\mu_{\boldsymbol{\Phi}}{\omega_{ib}}^2{\omega_s}^2 + \mu_\vartheta{\omega_a}^2\omega_{ib}{}^2 + \mu_\vartheta{\omega_a}^2{\omega_s}^2 + {\omega_a}^2{\omega_s}^2\right) q^2 \\ +2\,{\omega_s}^2\zeta_{ib}\mu_\vartheta{\omega_a}^2\omega_{ib}q + \mu_\vartheta{\omega_a}^2{\omega_{ib}}^2{\omega_s}^2 \end{pmatrix} \tag{44}$$

Using Eq. (39), the closed-form expression for $\Xi_n(\omega)$ has been derived as [107]

$$\begin{aligned}\Xi_6(\omega) = {} & 4\,\omega^6{\zeta_{ib}}^2{\mu_{\boldsymbol{\Phi}}}^2{\omega_{ib}}^2 + \left(-8\,{\zeta_{ib}}^2\mu_{\boldsymbol{\Phi}}\mu_\vartheta{\omega_a}^2{\omega_{ib}}^2 + {\mu_{\boldsymbol{\Phi}}}^2{\omega_{ib}}^4\right)\omega^4 \\ & + \left(4\,{\zeta_{ib}}^2{\mu_\vartheta}^2{\omega_a}^4{\omega_{ib}}^2 - 2\,\mu_{\boldsymbol{\Phi}}\mu_\vartheta{\omega_a}^2{\omega_{ib}}^4\right)\omega^2 + {\mu_\vartheta}^2{\omega_a}^4{\omega_{ib}}^4\end{aligned} \tag{45}$$

The standard deviation of the displacement response of the main system has been derived as

$${\sigma_{y_s}^2} = \frac{S_0\pi\,\omega_{ib}\begin{pmatrix}\left(4\,{\zeta_{ib}}^2\mu_\vartheta{\omega_s}^2 + \mu_\vartheta{\omega_{ib}}^2 + {\omega_s}^2\right){\omega_a}^2 \\ -4\,{\zeta_{ib}}^2\mu_{\boldsymbol{\Phi}}{\omega_s}^4 - \mu_{\boldsymbol{\Phi}}{\omega_{ib}}^2{\omega_s}^2 - {\omega_s}^4\end{pmatrix}}{2\zeta_{ib}\left({\omega_a}^2 - {\omega_s}^2\right){\omega_s}^6} \tag{46}$$

The extended form of the Eq. (46) has been written in Appendix A. After that, the standard deviation of velocity response of the main system has been derived as

$${\sigma_{\dot{y}_s}^2} = \frac{S_0\pi\omega_{ib}\begin{pmatrix}\left(4\,{\zeta_{ib}}^2\mu_\vartheta{\omega_s}^2 + 4\,{\zeta_{ib}}^2{\omega_s}^2 + \mu_\vartheta{\omega_{ib}}^2\right){\omega_a}^2 \\ -4\,{\zeta_{ib}}^2\mu_{\boldsymbol{\Phi}}{\omega_s}^4 - 4\,{\zeta_{ib}}^2{\omega_s}^4 - \mu_{\boldsymbol{\Phi}}{\omega_{ib}}^2{\omega_s}^2\end{pmatrix}}{2{\omega_s}^2\zeta_{ib}\left({\omega_a}^2 - {\omega_s}^2\right)} \tag{47}$$

The extended form of the Eq. (47) has been written in Appendix A. After that, the standard deviation of shear force of the whole isolated system has been derived as

$${\sigma_{sf}^2} = \frac{S_0\pi\,\omega_{ib}\begin{pmatrix}\left(4\,{\zeta_{ib}}^2\mu_\vartheta{\omega_s}^2 + \mu_\vartheta{\omega_{ib}}^2 + {\omega_s}^2\right){\omega_a}^2 \\ -4\,{\zeta_{ib}}^2\mu_{\boldsymbol{\Phi}}{\omega_s}^4 - \mu_{\boldsymbol{\Phi}}{\omega_{ib}}^2{\omega_s}^2 - {\omega_s}^4\end{pmatrix}}{2\zeta_{ib}\left({\omega_a}^2 - {\omega_s}^2\right){\omega_s}^2} \tag{48}$$

The extended form of the Eq. (48) has been written in Appendix A. Eq. (46) has been partially differentiated with respect to the damping ratio ζ_{ib} and frequency ω_{ib} of the novel isolators to obtain the exact closed-form expression for the optimal design parameters, respectively. Therefore, these optimal design parameters have been derived minimizing ${\sigma_{y_s}^2}$ which leads to

$$\frac{\partial\sigma_{y_s}^2}{\partial\zeta_{ib}} = 0 \quad \text{and} \quad \frac{\partial\sigma_{y_s}^2}{\partial\omega_{ib}} = 0 \tag{49}$$

Eq. (46) has been inserted into the first equation of Eq. (49). Therefore, the optimal damping ratio of the novel isolators has been derived as

$$(\zeta_{ib})_{opt} = \sqrt{\frac{\mu_\vartheta{\omega_a}^2{\omega_{ib}}^2 - \mu_{\boldsymbol{\Phi}}{\omega_{ib}}^2{\omega_s}^2 + {\omega_a}^2{\omega_s}^2 - {\omega_s}^4}{4\,\mu_\vartheta{\omega_a}^2{\omega_s}^2 - 4\,\mu_{\boldsymbol{\Phi}}{\omega_s}^4}} \tag{50}$$

Eq. (50) defines the optimal damping ratio of the novel isolators. However, this closed-form expression contains the frequency of the novel isolators ω_{ib}, which needs to be separated. To perform that, Eq. (50) has been substituted in Eq. (46). Now the modified value of ${\sigma_{y_s}^2}$ is expressed as

$${\sigma_{y_s}^2} = \frac{2\omega_{ib}\pi\,S_0\left(\mu_\vartheta{\omega_a}^2{\omega_{ib}}^2 - \mu_{\boldsymbol{\Phi}}{\omega_{ib}}^2{\omega_s}^2 + {\omega_a}^2{\omega_s}^2 - {\omega_s}^4\right)}{\left({\omega_a}^2 - {\omega_s}^2\right){\omega_s}^6\sqrt{\frac{\mu_{\boldsymbol{\Phi}}{\omega_{ib}}^2{\omega_s}^2 - \mu_\vartheta{\omega_a}^2{\omega_{ib}}^2 - {\omega_a}^2{\omega_s}^2 + {\omega_s}^4}{{\omega_s}^2\left(\mu_{\boldsymbol{\Phi}}{\omega_s}^2 - \mu_\vartheta{\omega_a}^2\right)}}} \tag{51}$$

Eq. (51) has been inserted into second constrains of Eq. (49) to obtain the optimal value of frequency of novel isolators ω_{ib}. Therefore, the optimal frequency of the novel isolators has been derived as

$$(\omega_{ib})_{opt} = \frac{\sqrt{2}\sqrt{\left(\mu_\vartheta{\omega_a}^2 - \mu_{\boldsymbol{\Phi}}{\omega_s}^2\right)\left({\omega_a}^2 - {\omega_s}^2\right)}\omega_s}{2(\mu_\vartheta{\omega_a}^2 - \mu_{\boldsymbol{\Phi}}{\omega_s}^2)} \tag{52}$$

The non-dimensional form of Eq. (52) has been listed in Appendix A. Eq. (52) has been substituted in Eq. (50). Therefore, the optimal damping ratio of the novel isolators has been derived as

$$(\zeta_{ib})_{opt} = 1/4\sqrt{\frac{6\,{\omega_a}^2 - 6\,{\omega_s}^2}{\mu_\vartheta{\omega_a}^2 - \mu_{\boldsymbol{\Phi}}{\omega_s}^2}} \tag{53}$$

The non-dimensional form of Eq. (53) has been listed in Appendix A. After substituting the values of $(\omega_{ib})_{opt}$ from Eq. (52) into Eq. (51), the optimal value of ${\sigma_{y_s}^2}$ has been obtained as

$$({\sigma_{y_s}^2})_{opt} = \frac{3\sqrt{2}S_0\pi\sqrt{\mu_\vartheta{\omega_a}^4 - {\omega_s}^2\left(\mu_{\boldsymbol{\Phi}} + \mu_\vartheta\right){\omega_a}^2 + \mu_{\boldsymbol{\Phi}}{\omega_s}^4}}{{\omega_s}^3\left(\mu_\vartheta{\omega_a}^2 - \mu_{\boldsymbol{\Phi}}{\omega_s}^2\right)\sqrt{\frac{6\,{\omega_a}^2 - 6\,{\omega_s}^2}{\mu_\vartheta{\omega_a}^2 - \mu_{\boldsymbol{\Phi}}{\omega_s}^2}}} \tag{54}$$

3.1. Sensitivity analysis of optimal design parameters

After deriving the closed-form expressions for the optimal frequency ratio η_{ib} and optimal damping ratio ζ_{ib} of novel isolators using H_2 optimization method, the sensitivity analysis of these parameters has been conducted to investigate the effectiveness of other system parameters on these optimal parameters, respectively. Fig. 4 shows the variation of optimal frequency ratio versus mass tuning ratio of the novel isolator. Precisely, Fig. 4(a) shows the variation of optimal frequency ratio versus mass tuning ratio of the novel isolators for different values of base mass ratio μ_{ib} and Fig. 4(b) shows the variation of optimal frequency ratio versus mass tuning ratio of the novel isolators for different values of inertial angle θ, respectively. Fig. 2(a) has already shown that the effective mass amplification occurred at $\theta \leq 30°$ and the significant amplification occurred at $\theta \leq 12°$. Therefore, these values of inertial angles have been considered as the critical inertial angle. For this particular reason, $\theta = 10°$ has been considered for most of the plots in this paper. Other system parameters have been considered as $\mu_T = 0.10$ and $\eta_a = 2$. The optimal frequency ratio increases gradually when the mass tuning ratio increases, indicating that the NSBI system (i.e., $\gamma = 0$) has a longer time period than the other two novel isolators.

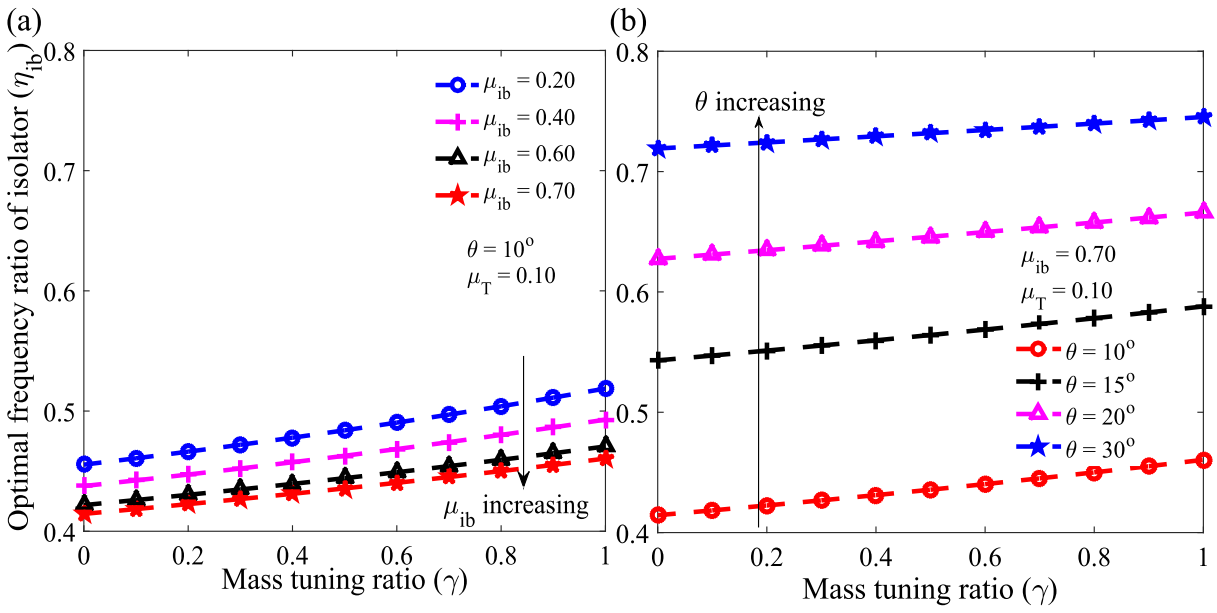

Fig. 4. (a) The variations of optimal frequency ratio η_{ib} versus mass tuning ratio γ of the novel isolators have been drawn for the different values of base mass ratio μ_{ib}. The blue ($\mu_{ib} = 0.20$), magenta ($\mu_{ib} = 0.40$), black ($\mu_{ib} = 0.60$) and red ($\mu_{ib} = 0.70$) lines with markers have been employed to indicate these plots. (b) The variations of optimal frequency ratio η_{ib} versus mass tuning ratio γ of the novel isolators have been plotted for the different values of inertial angle θ. The red ($\theta = 10°$), black ($\theta = 15°$), magenta ($\theta = 20°$), and blue ($\theta = 30°$) lines with markers have been employed to indicate these plots. For both graphs, other system parameters are considered as $\mu_T = 0.10$ and $\theta = 10°$.

This scenario is expected as the NSBI system contains only negative stiffness. The NSIABI systems (i.e., $0.10 < \gamma < 0.90$) have also contained lower frequency ratio than IABI system (i.e., $\gamma = 1.0$), respectively. This scenario happens because NSIABI systems preserve the combined effect of negative stiffness and inertial amplifier while IABI contains only inertial amplifiers. Overall, the lower mass tuning ratio provides a longer time period than the higher mass tuning ratio for isolated structures, respectively. Now, the optimal damping ratio trends for particular values of mass tuning ratio needs to be investigated. To perform that, the variation of optimal damping ratio versus mass tuning ratio of the novel isolator has been displayed in Fig. 5. The tendency of optimal damping ratio plots is the same as Fig. 4. The optimal damping ratio of the novel isolators gradually increases when the mass tuning ratio rises. It has already been proven that damping of the structure decreases its natural frequency from its absolute value. The NSBI system (i.e., $\gamma = 0$) provides an extended time period to isolated structures, decreasing the isolator's natural frequency. Hence, the lower natural frequency ratio of the isolator reduces the optimal damping of the NSBI system, whereas IABI has no effect of negative stiffness within it. Therefore, the natural frequency of the IABI did not distress while the damping is increasing due to the effect of amplification of effective mass. The damping of the NSIABI is also lower than IABI but higher than NSBI due to the combined effect of negative stiffness and inertial amplifier. Therefore, higher effective mass increases energy dissipation capacity than the extended time period. Due to that particular reason, the vibration reduction capacity of IABI is more than the NSBI and NSIABI, respectively.

For NSIABI systems, the variation of optimal design parameters versus base mass ratio needs to be investigated. To perform that, Fig. 6 has been drawn where Fig. 6(a) shows the variation of optimal frequency ratio versus base mass ratio for different values of θ. The optimal frequency ratio of the isolator decreases when the base mass ratio of the NSIABI increases. Therefore, the higher base mass ratio has extended the time period of the isolated structures more than the lower base mass ratio. Interestingly, a lower inertial angle (i.e. $\theta = 10°$) provides a feasible frequency ratio for the isolator. In contrast, the higher inertial angles (i.e. $\theta \geq 20°$) reduce the flexibility of the isolated structure compared to the lower one. The time period of the isolated structure decreases due to that particular reason. Additionally, the lower base mass ratio with a higher angle provides a higher frequency ratio, and the time period of the isolator has been over condensed. It has over reduced the flexibility to the base of the NSIABI, which may damage its base. The ductile property of the isolator has been shrunken. Finally, $\theta \leq 10°$ has been considered optimal inertial angle, which provides optimal flexibility as well as sufficient load-bearing capacity to the isolated structure, respectively. Fig. 6(b) shows the variation of optimal damping ratio versus base mass ratio for different values of θ. The optimal damping ratio of the isolator decreases when the base mass ratio of the NSIABI increases. Hence, the higher base mass ratio provides optimal lower damping for the novel isolators, which is feasible and can also be implemented for practical design purposes. The lower base mass ratio of NSIABI provides higher damping, which is not cost-effective. Apart from that, a lower base mass ratio with higher damping provides extended damping, making the isolated structure overdamped. Therefore, a higher base mass ratio has been recommended for the optimal design of the NSIABI system. Now considering the optimal inertial angle (i.e., $\theta = 10°$, the same type of plots have been configured for NSBI and IABI systems, respectively. Fig. 7(a) shows the variation of optimal frequency ratio versus the base mass ratio of the novel isolators. This figure depicts that the optimal frequency ratio decreases when the base mass ratio increases. Overall the optimal frequency ratios of the NSBI system is much lesser than the other NSIABI and IABI system due to the effect of negative stiffness. As expected, structures isolated by NSBI have a more extended time period than the other two isolated systems. The same effect has been observed in Fig. 7(b), where the variation of optimal damping ratio versus the base mass ratio of the novel isolators have been displayed. The optimal damping ratio of each isolator decreases while the base mass ratio increases. In the previous plots, it has already been observed that a higher base mass ratio provides a robust design for all three novel isolators. The damping ratios of IABI is more than the other two isolators, while NSBI is the lowest one. The mass amplification effect of inertial amplifiers plays the primary role in amplifying the dissipation energy of the isolated structures. However, the static mass does not affect that. Only the effective mass plays a crucial part, whereas, in the NSBI system, the mass amplification is near to zero. These optimal damping ratios can

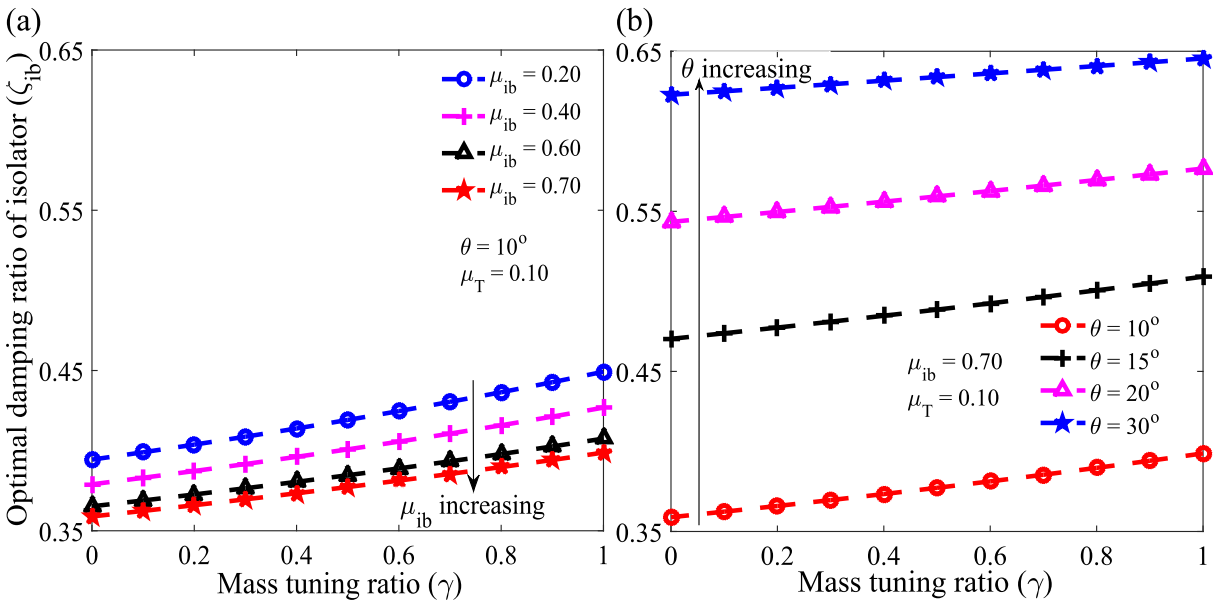

Fig. 5. (a) The variations of optimal damping ratio ζ_{ib} versus mass tuning ratio γ of the novel isolators have been plotted for the different values of base mass ratio μ_{ib}. The blue ($\mu_{ib} = 0.20$), magenta ($\mu_{ib} = 0.40$), black ($\mu_{ib} = 0.60$) and red ($\mu_{ib} = 0.70$) lines with markers have been employed to indicate these plots. (b) The variations of optimal damping ratio ζ_{ib} versus mass tuning ratio γ of the novel isolators have been plotted for the different values of inertial angle θ. The red ($\theta = 10°$), black ($\theta = 15°$), magenta ($\theta = 20°$), and blue ($\theta = 30°$) lines with markers have been employed to indicate these plots. For both graphs, other system parameters are considered as $\mu_T = 0.10$ and $\theta = 10°$.

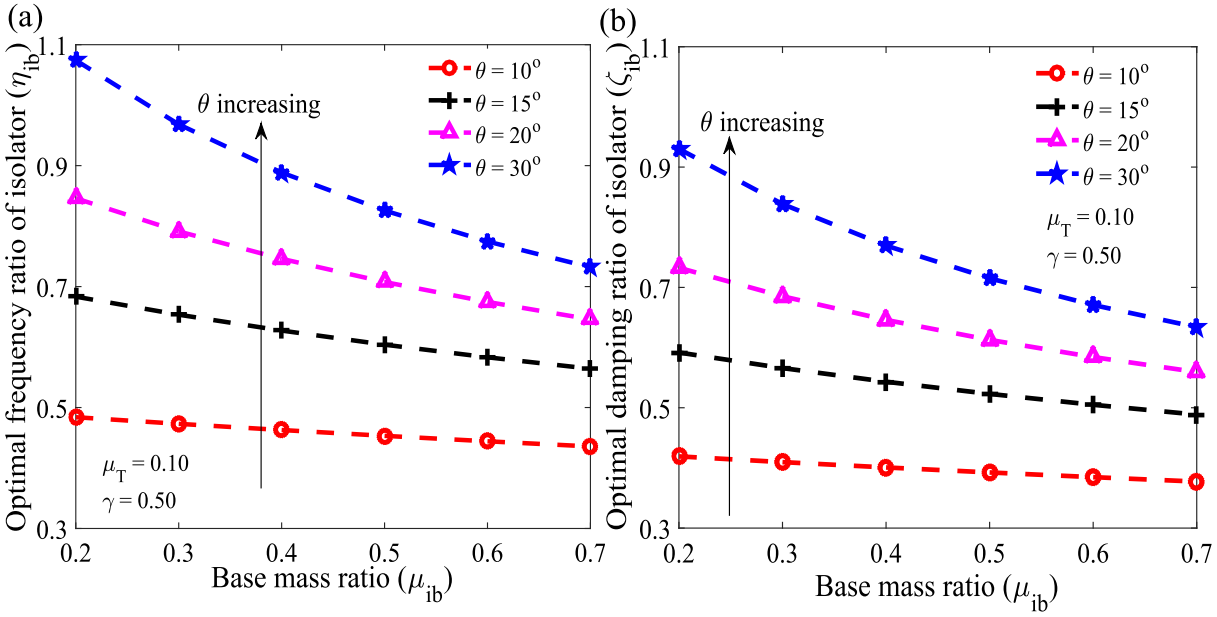

Fig. 6. (a) The variations of optimal frequency ratio η_{ib} versus base mass ratio μ_{ib} of the NSIABI system have been plotted for different values of inertial angle θ. (b) The variations of optimal damping ratio ζ_{ib} versus base mass ratio μ_{ib} of the NSIABI system have been plotted for different values of inertial angle θ. For both graphs, the red ($\theta = 10°$), black ($\theta = 15°$), magenta ($\theta = 20°$), and blue ($\theta = 30°$) lines with markers have been employed to indicate each plot. Other system parameters are considered as $\mu_T = 0.10$ and $\gamma = 0.50$.

also be located at Fig. 8 where the variation of the standard deviation of displacement of main structure versus damping ratio of novel isolators has been shown. Eq. (46) have been applied to plot these graphs, and from this equation, the closed-form expressions for optimal frequency and damping ratio novel isolators have been derived, respectively. The Fig. 8 has been added to maintain the work's transparency and cross-check the accuracy of the results presented before. Fig. 8(a) displays the variation of the standard deviation of displacement of the main structure isolated by NSBI. For each base mass ratio, optimal frequency ratio has been obtained using Eq. (A.6). The optimal standard deviation plots have been achieved using these optimal values. As the input values are optimum, the damping ratios located from the plot are optimum. The same type of plots for structures isolated by NSIABI and IABI has been shown in Fig. 8(b) and Fig. 8(c). The values of optimal damping ratios located from Fig. 8 are exactly matched with the optimal damping values derived from Eq. (A.7). Hence, the newly introduced closed-form expressions are 100% accurate and can be used for practical design purposes, respectively. Using these optimal design parameters, the robustness of the novel isolators have been shown Fig. 9. The variation of displacement of the main structure isolated by each novel isolator has been displayed in Fig. 9. The displacement of the main structure is unrestrained at $\zeta_{ib} = 0$. The displacement of the structure has been mitigated at resonating frequency when the damping ratio of the novel isolators increases. The resonating, minimum/minima [108],

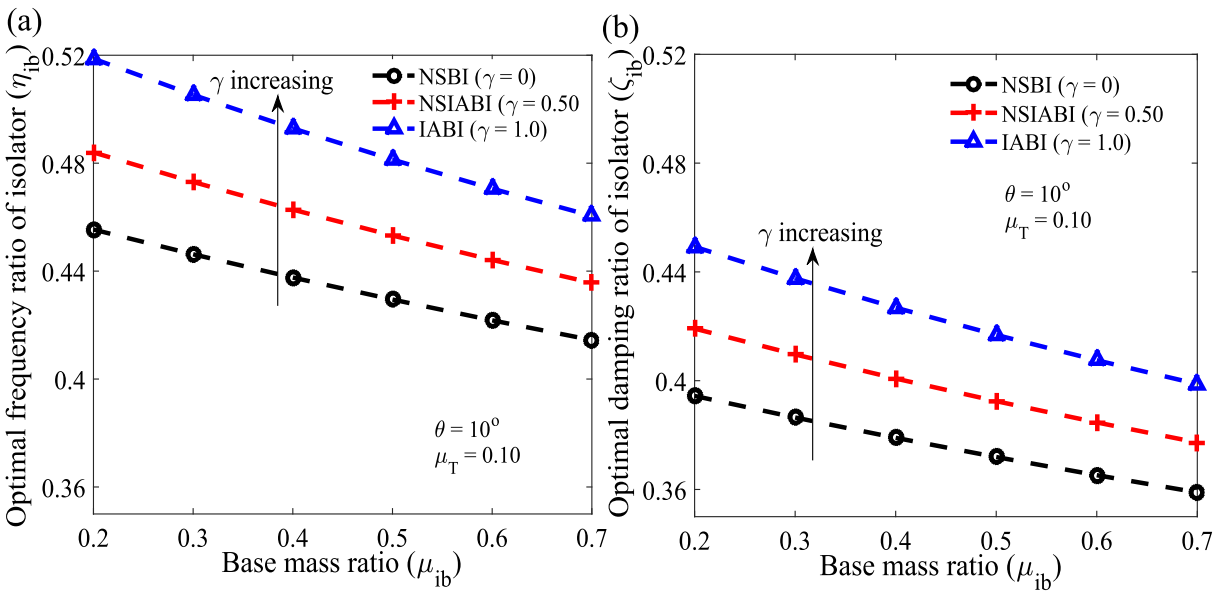

Fig. 7. (a) The variations of optimal frequency ratio η_{ib} versus base mass ratio μ_{ib} of the novel isolators have been plotted for different values of mass tuning ratio γ. (b) The variations of optimal damping ratio ζ_{ib} versus base mass ratio μ_{ib} of the novel isolators have been plotted for different values of mass tuning ratio γ. For both graphs, the black ($\gamma = 0$), red ($\gamma = 0.5$), and blue ($\gamma = 1.0$) lines with markers have been employed to indicate these plots for each isolator (i.e., NSBI, NSIABI, IABI). Other system parameters are considered as $\mu_T = 0.10$ and $\theta = 10°$.

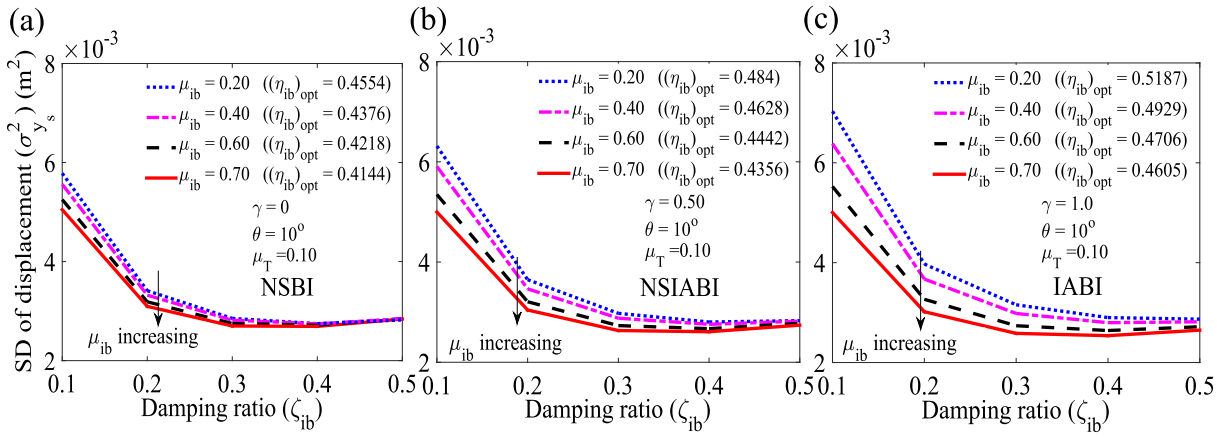

Fig. 8. The variations of the standard deviation (SD) of displacement for structures isolated by (a) NSBI ($\gamma = 0$), (b) NSIABI ($\gamma = 0.50$), and (c) IABI ($\gamma = 1.0$) versus damping ratio of the novel isolators have been plotted for different values of base mass ratio μ_{ib}. For all graphs, the blue dotted ($\mu_{ib} = 0.20$), magenta dash-dotted ($\mu_{ib} = 0.40$), black dash–dash ($\mu_{ib} = 0.60$) and red ($\mu_{ib} = 0.70$) lines have been employed to indicate each plot. Eq. (A.6) is employed for inducing the optimal frequency ratio for each plot.

and anti-resonating regions can be located from this plot. In Fig. 9(a) and (b), the frequency region of all three peaks refers to each resonating frequency, and the smallest point between two consecutive resonances refers as minimum/minima. The maximum response drop has been located at the anti-resonance frequency region. The maximum values of structural displacements have been derived and displayed in each graph. All the peaks merged into one when the damping of the isolators tends to infinity (i.e., $\zeta_{ib} = \infty$). Therefore, the plots of the main structure and novel isolator bind together. Due to that, each controlled structure is shortened to a single degree of freedom system (SDOF). For Fig. 9(c), in the IABI system, only one minimum/minima and two resonance frequencies can be observed because the effective properties (mass and stiffness) are not frequency-dependent. On the other hand, in NSIABI and NSBI, one anti-resonance, one minimum/minima and three resonance peaks can be noticed as the effective properties (mass and stiffness) are frequency-dependent.

4. H_∞ Optimization for harmonic excitation

The H_∞ optimization has been performed to minimize the maximum amplitude of the frequency responses based on the fixed-point theory [109]. Thus, when these controlled systems are subjected to harmonic excitations instead of white-noise random excitations, the H_∞ optimization method is more effective than H_2 norm. Therefore, the closed-form expressions for optimal design parameters of the novel isolators have been derived using this optimization method. To perform the H_∞ optimization method, Eq. (19) has been converted in to non-dimensional form. Hence, the modified Eq. (19) has been expressed as

$$\begin{bmatrix} 2i\eta\zeta_s - \eta^2 + 1 & -\eta^2 \\ -2i\eta\zeta_s - 1 & \frac{(2i\eta\zeta_{ib}\eta_{ib} - \eta^2 + \eta_{ib}^2)(\eta^2\mu_\Phi - \eta_a{}^2\mu_\vartheta)}{\eta^2 - \eta_a{}^2} \end{bmatrix} \begin{Bmatrix} Y_s \\ Y_{ib} \end{Bmatrix} = -\begin{bmatrix} 1 \\ \mu_{ia} \end{bmatrix} \frac{U_g}{\omega_s^2} \tag{55}$$

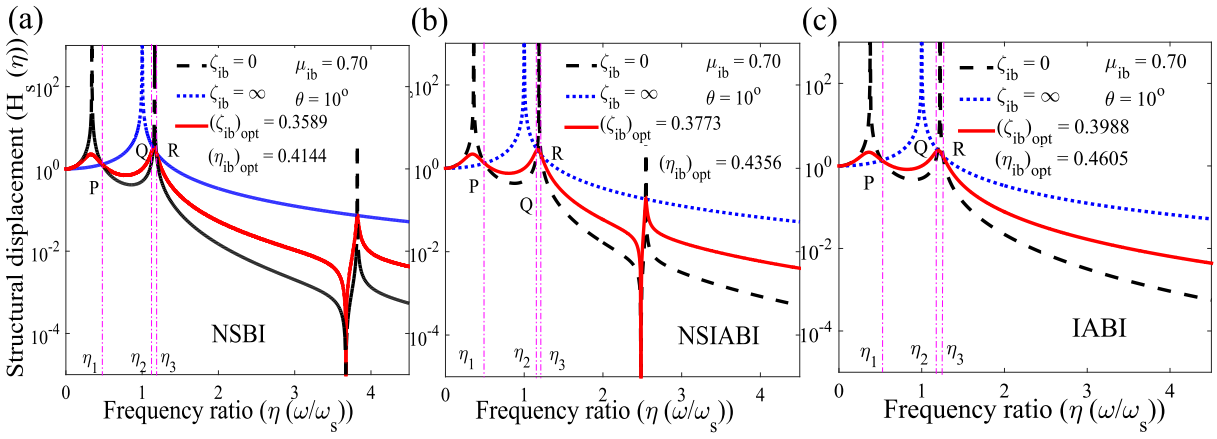

Fig. 9. The variations of the displacement of the main structure $H_s(\eta)$ isolated by (a) NSBI ($\gamma = 0$), (b) NSIABI ($\gamma = 0.50$), and (c) IABI ($\gamma = 1.0$) versus frequency ratio have been plotted for different values of damping ratio of novel isolators. The black dash, blue dotted, and red lines have been implemented to address the displacement plots for damping ratio of 0, ∞, and $(\zeta_{ib})_{opt}$. Eqs. (A.6) and (A.7) have been applied to obtain the optimal frequency and damping ratio of the novel isolators, which have been applied to plot these graphs. Other system parameters are considered as $\mu_{ib} = 0.70$ and $\theta = 10°$. For all graphs, P, Q, and R are indicating three fixed points, and the corresponding frequency ratios are denoted as η_1, η_2, and η_3.

where $\mu_{ia} = (\eta^2\mu_\Phi - \eta_a{}^2\mu_\vartheta)/(\eta^2 - \eta_a{}^2)$, defines as the ratio of total effective mass to the mass of the main structure. The displacement response of the main structure has been derived as

$$H_s(\eta) = \frac{Y_s}{U_g}\omega_s^2 = \frac{\left(\eta^2\mu_\Phi - \eta_a{}^2\mu_\vartheta\right)\left(\eta_{ib}{}^2 + 2i\eta\,\zeta_{ib}\eta_{ib}\right)}{\Delta_n} \tag{56}$$

The displacement response of the novel isolators has been derived as

$$H_{ib}(\eta) = \frac{Y_{ib}}{U_g}\omega_s^2 = \frac{\begin{pmatrix} -\eta^4\mu_\Phi + \eta^2\eta_a{}^2\mu_\vartheta + \eta^2\mu_\Phi - \eta_a{}^2\mu_\vartheta + \eta^2 \\ -\eta_a{}^2 + 2i\zeta_s\eta\left(\eta^2\left(\mu_\Phi + 1\right) - \eta_a{}^2\left(\mu_\vartheta + 1\right)\right) \end{pmatrix}}{\Delta_n} \tag{57}$$

The closed-form expression for Δ_n has been derived as

$$\Delta_n = \begin{pmatrix} -\eta^6\mu_\Phi + \left(2i\mu_\Phi\eta_{ib}\zeta_{ib} + 2i\zeta_s\mu_\Phi + 2i\zeta_s\right)\eta^5 \\ +\left(4\,\zeta_{ib}\zeta_s\eta_{ib}\mu_\Phi + \eta_a{}^2\mu_\vartheta + \eta_{ib}{}^2\mu_\Phi + \mu_\Phi + 1\right)\eta^4 \\ -2i\left(\left(\eta_{ib}{}^2\mu_\Phi + \eta_a{}^2\left(\mu_\vartheta + 1\right)\right)\zeta_s + \eta_{ib}\zeta_{ib}\left(\eta_a{}^2\mu_\vartheta + \mu_\Phi\right)\right)\eta^3 \\ -\left(4\,\eta_a{}^2\zeta_s\eta_{ib}\zeta_{ib}\mu_\vartheta + \eta_a{}^2\eta_{ib}{}^2\mu_\vartheta + \eta_a{}^2\mu_\vartheta + \eta_{ib}{}^2\mu_\Phi + \eta_a{}^2\right)\eta^2 \\ +2i\eta_a{}^2\mu_\vartheta\eta_{ib}\left(\zeta_s\eta_{ib} + \zeta_{ib}\right)\eta + \eta_a{}^2\eta_{ib}{}^2\mu_\vartheta \end{pmatrix} \tag{58}$$

To apply the fixed-point theory considers $\zeta_s = 0$ and the closed-form expression of the $H_s(\eta)$ has been modified as

$$H_s(\eta)_{\zeta_s=0} = \frac{Y_s}{U_g}\omega_s^2 = \frac{\left(\eta^2\mu_\Phi - \eta_a{}^2\mu_\vartheta\right)\left(\eta_{ib}{}^2 + 2i\eta\,\zeta_{ib}\eta_{ib}\right)}{\Delta_n|_{\zeta_s=0}} \tag{59}$$

Simultaneously, the closed-form expression of the Δ_n has been modified as

$$\Delta_n|_{\zeta_s=0} = \begin{pmatrix} -\eta^6\mu_\Phi + \left(\eta_a{}^2\mu_\vartheta + \eta_{ib}{}^2\mu_\Phi + \mu_\Phi + 1\right)\eta^4 \\ +\left(-\eta_a{}^2\eta_{ib}{}^2\mu_\vartheta - \eta_a{}^2\mu_\vartheta - \eta_{ib}{}^2\mu_\Phi - \eta_a{}^2\right)\eta^2 \\ +\eta_a{}^2\eta_{ib}{}^2\mu_\vartheta + 2i\left(\eta^2\mu_\Phi - \eta_a{}^2\mu_\vartheta\right)\eta\,(\eta+1)(\eta-1)\,\zeta_{ib}\eta_{ib} \end{pmatrix} \tag{60}$$

To minimize the maximum amplitude of the displacement response of the main structure, the modulus of $H_s(\eta)$ has been derived and expressed as

$$|H_s(\eta)| = \sqrt{\frac{R_s^2 + \zeta_{ib}^2 I_s^2}{P_r^2 + \zeta_{ib}^2 Q_i^2}} = \left|\frac{I_s}{Q_i}\right|\sqrt{\frac{\left(\frac{R_s}{I_s}\right)^2 + \zeta_{ib}^2}{\left(\frac{P_r}{Q_i}\right)^2 + \zeta_{ib}^2}} \tag{61}$$

where

$$R_s = \eta_{ib}{}^2\left(\eta^2\mu_\Phi - \mu_\vartheta\eta_a{}^2\right), I_s = 2\,\eta\,\eta_{ib}\left(\eta^2\mu_\Phi - \mu_\vartheta\eta_a{}^2\right)$$

$$P_r = \begin{pmatrix} -\eta^6\mu_\Phi + \left(\mu_\vartheta\eta_a{}^2 + \eta_{ib}{}^2\mu_\Phi + \mu_\Phi + 1\right)\eta^4 \\ +\left(\left(-\eta_{ib}{}^2\mu_\vartheta - \mu_\vartheta - 1\right)\eta_a{}^2 - \eta_{ib}{}^2\mu_\Phi\right)\eta^2 + \eta_a{}^2\eta_{ib}{}^2\mu_\vartheta \end{pmatrix} \tag{62}$$

$$Q_i = 2\,\eta\,\eta_{ib}\,(\eta-1)(\eta+1)\left(\eta^2\mu_\Phi - \mu_\vartheta\eta_a{}^2\right)$$

Two constraints have been applied to derive the optimal frequency and damping ratio of the novel isolators using the fixed point theory [27]. These constraints are listed below.

$$\left(\frac{R_s}{I_s}\right)^2\Big|_{\eta_j} = \left(\frac{P_r}{Q_i}\right)^2\Big|_{\eta_j} \quad \text{and} \quad \left(\frac{I_s}{Q_i}\right)^2\Big|_{\eta_1} = \left(\frac{I_s}{Q_i}\right)^2\Big|_{\eta_2} \tag{63}$$

Now applying the first constraint, the values of $\eta_{1,2,3}$ have been obtained as [109]

$$\begin{matrix} \eta^6\mu_\Phi + \left(-\mu_\vartheta\eta_a{}^2 - 2\,\eta_{ib}{}^2\mu_\Phi - \mu_\Phi - 1\right)\eta^4 \\ +\left(\left(2\,\eta_{ib}{}^2\mu_\vartheta + \mu_\vartheta + 1\right)\eta_a{}^2 + 2\,\eta_{ib}{}^2\mu_\Phi\right)\eta^2 - 2\,\eta_a{}^2\eta_{ib}{}^2\mu_\vartheta \end{matrix} = 0 \tag{64}$$

It can also be noted that $\eta_3 > \eta_2 > \eta_1$ and the values are obtained as [110]:

$$\eta_1^2 + \eta_2^2 + \eta_3^2 = \frac{\mu_\vartheta\eta_a{}^2}{\mu_\Phi} + 2\,\eta_{ib}{}^2 + 1 + \frac{1}{\mu_\Phi} \tag{65}$$

$$\eta_1^2\eta_2^2\eta_3^2 = \frac{2\eta_a{}^2\eta_{ib}{}^2\mu_\vartheta}{\mu_\Phi} \tag{66}$$

$$\eta_1^2\eta_2^2 + \eta_1^2\eta_3^2 + \eta_2^2\eta_3^2 = \frac{\left(2\,\eta_{ib}{}^2\mu_\vartheta + \mu_\vartheta + 1\right)\eta_a{}^2 + 2\,\eta_{ib}{}^2\mu_\Phi}{\mu_\Phi} \tag{67}$$

To get the values of η_1 and η_2, the second constraints in Eq. (63) need to be implemented as $\zeta_{ib} = \infty$. Using second constraint in Eq. (63),

$$\eta_1{}^2 + \eta_2{}^2 = 2 \tag{68}$$

Now, substitute Eq. (68) into first equation of Eq. (65) which leads to

$$\eta_3^2 = \frac{\mu_\vartheta\eta_a{}^2}{\mu_\Phi} + 2\,\eta_{ib}{}^2 + \frac{1}{\mu_\Phi} - 1 \tag{69}$$

In order to find the optimal frequency ratio of the novel isolators, Eq. (69) have been substituted in Eq. (66) and Eq. (67). A equation have been generated using the second constraints of Eq. (63), and Eq. (66), Eq. (67) which contains the closed-form expression of optimal frequency ratio of the novel isolators, respectively. Therefore, the equation have been derived as

$$\begin{matrix} \left(-4\,\eta_a{}^2\mu_\Phi\mu_\vartheta + 4\,\mu_\Phi{}^2\right)\eta_{ib}{}^4 \\ +\ \left(-2\,\eta_a{}^4\mu_\vartheta{}^2 + 8\,\eta_a{}^2\mu_\Phi\mu_\vartheta - 2\,\eta_a{}^2\mu_\Phi - 2\,\eta_a{}^2\mu_\vartheta - 6\,\mu_\Phi{}^2 + 6\,\mu_\Phi\right)\eta_{ib}{}^2 \\ +\,\eta_a{}^4\mu_\vartheta{}^2 - \eta_a{}^4\mu_\vartheta - 3\,\eta_a{}^2\mu_\Phi\mu_\vartheta + \eta_a{}^2\mu_\Phi + 3\,\eta_a{}^2\mu_\vartheta - \eta_a{}^2 \\ +\,2\,\mu_\Phi{}^2 - 4\,\mu_\Phi + 2 = 0 \end{matrix} \tag{70}$$

Considers $x = \eta_{ib}^2$ and Eq. (70) has been written as

$$w_2x^2 + w_1x + w_0 = 0 \tag{71}$$

The values of w_2, w_1, and w_0 have been listed in Appendix B. Eq. (71) is a quadratic equation which has been solved as

$$x = \frac{-w_1 \pm \sqrt{w_1^2 - 4w_2w_0}}{2w_2} \tag{72}$$

Therefore, using Eq. (72), the closed-form expression for optimum η_{ib} has been derived as

$$(\eta_{ib})^2_{opt} = \frac{\left(\begin{array}{c} -{\eta_a}^4{\mu_\vartheta}^2 + 4\,{\eta_a}^2\mu_\Phi\mu_\vartheta - {\eta_a}^2\mu_\Phi - {\eta_a}^2\mu_\vartheta - 3\,{\mu_\Phi}^2 + 3\,\mu_\Phi \\ + \sqrt{\left(\begin{array}{c} {\eta_a}^8{\mu_\vartheta}^4 - 4\,{\eta_a}^6\left(\mu_\Phi - 1/2\right)\mu_\vartheta{}^3 \\ -2\left({\eta_a}^2\mu_\Phi - 3\,{\mu_\Phi}^2 + \mu_\Phi - 1/2\right){\eta_a}^4{\mu_\vartheta}^2 \\ -2\,{\eta_a}^2\mu_\Phi\left({\eta_a}^2 + 2\,{\mu_\Phi}^2 - \mu_\Phi - 1\right)\mu_\vartheta \\ +{\mu_\Phi}^2\left({\eta_a}^2 + \mu_\Phi - 1\right)^2 \end{array} \right)} \end{array} \right)}{4\,\mu_\Phi\left({\eta_a}^2\mu_\vartheta - \mu_\Phi\right)} \tag{73}$$

Now, in order to derive the closed-form expression for optimal damping ratio of the novel isolators, the value of η_1^2 and η_2^2 needs to be obtained. Hence, using Eq. (65), Eq. (66), Eq. (67), and Eq. (69), the value of η_1^2 and η_2^2 has been derived as

$$\eta_{1,2}^2 = 1 \pm \sqrt{\frac{-2\,{\eta_{ib}}^2{\eta_a}^2\mu_\vartheta + 2\,{\eta_{ib}}^2\mu_\Phi + {\eta_a}^2\mu_\vartheta - \mu_\Phi + 1}{2\,{\eta_{ib}}^2\mu_\Phi + {\eta_a}^2\mu_\vartheta - \mu_\Phi + 1}} \tag{74}$$

To obtain the optimal value of $\eta_{1,2}^2$, Eq. (73) has been substituted in Eq. (74). Now, Eq. (73) has been substituted in Eq. (61) and squared this expression to derive the optimal damping ratio of the novel isolators. Therefore, the closed-form expression for optimal ζ_{ib} has been obtained by solving the following equations

$$\frac{\partial|H_s(\eta)|^2}{\partial\eta^2}|_{\eta_{1,2}^2} = 0 \quad \text{and} \quad (\zeta_{ib})_{opt} = \sqrt{\frac{\zeta_{ib1}^2 + \zeta_{ib2}^2}{2}} \tag{75}$$

Using Eq. (75), the viscous damping ratios of the novel isolators ζ_{ib1}^2, ζ_{ib2}^2 for the corresponding values of η_1^2, η_2^2 have been derived as

$$\begin{array}{c} -3\,\eta_{1,2}^{10}{\mu_\Phi}^2 \\ +\left(5\,{\eta_{ib}}^2{\mu_\Phi}^2 + 5\,{\eta_a}^2\mu_\Phi\mu_\vartheta + 5\,{\mu_\Phi}^2 + 5\,\mu_\Phi\right)\eta_{1,2}^8 \\ +\left(\begin{array}{c} -{\eta_{ib}}^4{\mu_\Phi}^2 - 8\,{\eta_{ib}}^2{\eta_a}^2\mu_\Phi\mu_\vartheta - 2\,{\eta_a}^4{\mu_\vartheta}^2 \\ -8\,{\eta_{ib}}^2{\mu_\Phi}^2 - 8\,{\eta_a}^2\mu_\Phi\mu_\vartheta - 4\,{\eta_{ib}}^2\mu_\Phi \\ -4\,{\eta_a}^2\mu_\Phi - 4\,{\eta_a}^2\mu_\vartheta - 2\,{\mu_\Phi}^2 \\ -4\,\mu_\Phi - 2 \end{array} \right)\eta_{1,2}^6 \\ +\left(\begin{array}{c} 2\,{\eta_{ib}}^4{\eta_a}^2\mu_\Phi\mu_\vartheta + 3\,{\eta_{ib}}^2{\eta_a}^4{\mu_\vartheta}^2 + {\eta_{ib}}^4{\mu_\Phi}^2 \\ +12\,{\eta_{ib}}^2{\eta_a}^2\mu_\Phi\mu_\vartheta + 3\,{\eta_a}^4{\mu_\vartheta}^2 + 3\,{\eta_{ib}}^2{\eta_a}^2\mu_\Phi \\ +3\,{\eta_{ib}}^2{\eta_a}^2\mu_\vartheta + 3\,{\eta_a}^4\mu_\vartheta + 3\,{\eta_{ib}}^2{\mu_\Phi}^2 \\ +3\,{\eta_a}^2\mu_\Phi\mu_\vartheta + 3\,{\eta_{ib}}^2\mu_\Phi + 3\,{\eta_a}^2\mu_\Phi \\ +3\,{\eta_a}^2\mu_\vartheta + 3\,{\eta_a}^2 \end{array} \right)\eta_{1,2}^4 \\ +\left(\begin{array}{c} -{\eta_{ib}}^4{\eta_a}^4{\mu_\vartheta}^2 - 2\,{\eta_{ib}}^4{\eta_a}^2\mu_\Phi\mu_\vartheta - 4\,{\eta_{ib}}^2{\eta_a}^4{\mu_\vartheta}^2 \\ -2\,{\eta_{ib}}^2{\eta_a}^4\mu_\vartheta - 4\,{\eta_{ib}}^2{\eta_a}^2\mu_\Phi\mu_\vartheta - {\eta_a}^4{\mu_\vartheta}^2 \\ -2\,{\eta_{ib}}^2{\eta_a}^2\mu_\Phi - 2\,{\eta_{ib}}^2{\eta_a}^2\mu_\vartheta \\ -2\,{\eta_a}^4\mu_\vartheta - {\eta_a}^4 \end{array} \right)\eta_{1,2}^2 \\ \zeta_{ib1,ib2}^2 = \dfrac{+{\eta_{ib}}^4{\eta_a}^4{\mu_\vartheta}^2 + {\eta_{ib}}^2{\eta_a}^4{\mu_\vartheta}^2 + {\eta_{ib}}^2{\eta_a}^4\mu_\vartheta}{4\,\eta_{1,2}^2{\eta_{ib}}^2\left(\begin{array}{c} \eta_{1,2}^2{\eta_a}^4{\mu_\vartheta}^2 - 2\,\eta_{1,2}^4{\eta_a}^2\mu_\Phi\mu_\vartheta - {\eta_a}^4{\mu_\vartheta}^2 \\ +\eta_{1,2}^6{\mu_\Phi}^2 + 2\,\eta_{1,2}^2{\eta_a}^2\mu_\Phi\mu_\vartheta - \eta_{1,2}^4{\mu_\Phi}^2 \end{array} \right)} \end{array} \tag{76}$$

Now, Eq. (76) has been substituted into the second expression of Eq. (75). Therefore, the optimal damping ratio of the novel isolators has been derived using the second expression of Eq. (75). Fig. 10 shows the variation of displacement of main structure versus frequency ratio for different values of ζ_{ib}. To plot Fig. 10, the system parameters are considered as $\zeta_s = 0$, $\mu_{ib} = 0.7$, $\gamma = 0.5$, $\theta = 10°$, $\eta_a = 2$, and $\mu_T = 0.10$ and the optimal frequency ratio η_{ib} and damping ratio ζ_{ib} have been obtained as 0.5822 and 0.4 using Eq. (73), Eq. (76), and Eq. (75). Same plots for structures controlled by NSBI and IABI systems have been displayed in Appendix C to provide a clear visualization. Two fixed points can easily be located from Fig. 10 as the optimal frequency ratio has been employed. The displacement of the main structure is unrestrained at $\zeta_{ib} = 0$. The displacement amplitude of the transfer function of the main structure and NSIABI are unbounded at its eigen frequencies (i.e., $\eta = 0.4702, 1.208, 2.546$), respectively. The responses throughout the system resonances have been attenuated when the damping ratio of the NSIABI system increases. The resonating, minimum/minima [108], and anti-resonating regions can be located from this plot. In Fig. 10, the frequency region of all three peaks refers to each resonating frequency (i.e., $\eta = 0.4664, 1.176, 2.546$), and the smallest point between two consecutive resonances refers to minimum/minima [108]. The maximum response drop has been located at the anti-resonance frequency region. The receptance of $H_s(\eta)$ has become zero at anti-resonance frequency (i.e., $\eta = 2.484$). Whereas, the receptance of $H_s(\eta)$ is not zero between two consecutive resonating frequencies (i.e., $\eta = 0.4664, 1.176$). That frequency region is indicated as minimum frequency (i.e., $\eta = 0.8444$). The log plot has only been implemented to address the resonating, minimum, and anti-resonating frequency. The maximum values of structural displacements have been derived and displayed in Fig. 10. Therefore, at optimal damping ratio $\zeta_{ib} = 0.4$, the maximum displacement amplitude is determined as 2.7994. All the peaks merged into one when the damping of the isolators tended to infinity (i.e., $\zeta_{ib} = \infty$). Therefore, the plots of the main structure and novel isolator bind together. Due to that, each controlled structure is shortened to a single degree of freedom system (SDOF). Therefore, a single peak has been observed from Fig. 10. For Fig. C.17(b), in the IABI system, only one minimum/minima and two resonance frequencies can be observed because the effective properties (mass and stiffness) are not frequency-dependent. On the other hand, in NSIABI and NSBI, one anti-resonance, one minimum/minima and three resonance peaks can be noticed as the effective properties (mass and stiffness) are frequency-dependent. In fact, it is also observed that for damping ratios less than 40%, the peak displacement amplitude decreases, and it becomes pretty stable and approximately constant for higher damping values. In addition, the plots of $H_s(\eta)$ at optimal η_{ib} coincide with each other when the damping of the isolator ζ_{ib} reached the value of 0.40. Therefore, $\zeta_{ib} = 0.40$ is considered as the optimal damping for proposed NSIABI systems, and this value is feasible for practical design purposes.

Fig. 11(a) shows the variation of optimal frequency ratio versus the base mass ratio of the novel isolators. This figure depicts that the optimal frequency ratio slightly increases when the base mass ratio increases. However, the variation of optimal frequency ratio from lower to higher bass mass ratio is minor. Overall the optimal frequency ratios of the IABI system is lesser than the other NSBI and NSIABI system due to the effect of effective mass amplification. However, the difference between optimal frequency ratios of IABI and NSBI was obtained as 12.13%. In contrast, the difference between IABI and NSIABI was obtained as 7.83%, which is low. Here, the effective mass amplification effect of the inertial amplifier plays a crucial role. The opposite effect has been observed in Fig. 11(b), where the variation of optimal damping ratio versus the base mass ratio of the novel isolators have been displayed. The optimal damping ratio of each isolator decreases while the base mass ratio increases. The previous section has already been observed that a higher base mass ratio provides a robust design for all three novel isolators. Overall the optimal damping ratio of the NSBI system is lesser than the other NSIABI and IABI system due to the effect of negative stiffness and more extended time period than other systems, respectively. The mass amplification effect of inertial amplifiers plays the primary role in amplifying the dissipation energy of the isolated structures. However, the static mass does not affect that. Only the effective mass plays a crucial part, whereas, in the NSBI system, the mass amplification is near to zero. NSIABI system provides a feasible design as the isolated structure is neither overdamped nor underdamped. Finally, all proposed isolators are robust, and a higher base mass ratio has been recommended for the robust

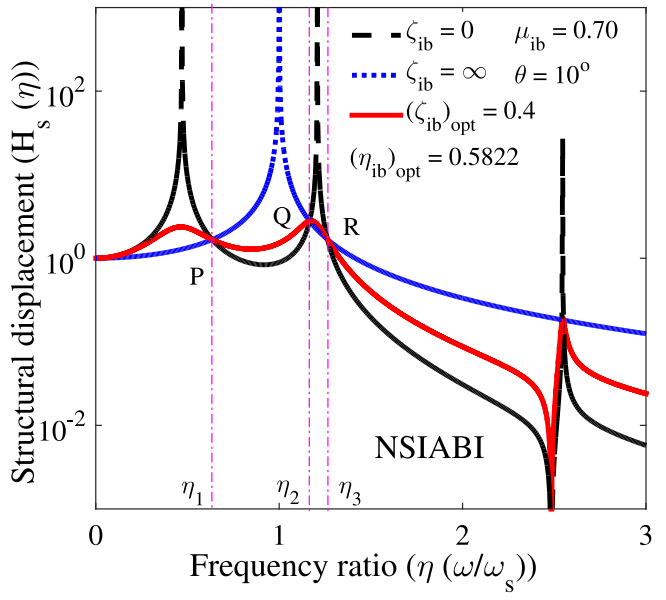

Fig. 10. The variations of displacement of the main structure $H_s(\eta)$ isolated by the NSIABI ($\gamma = 0.50$) versus frequency ratio $\eta(\omega/\omega_s)$ have been plotted for different values of damping ratio of the NSIABI system. The black dash, blue dotted, and red lines have been implemented to address the displacement plots for damping ratio of 0, ∞, and $(\zeta_{ib})_{opt}$. Eqs. (73), (75) and (76) have been applied to obtain the optimal frequency and damping ratio of the NSIABI system, which have been applied to plot this graph. Other system parameters are considered as $\mu_{ib} = 0.70$ and $\theta = 10°$. For all graphs, P, Q, and R are indicating three fixed points, and the corresponding frequency ratios are denoted as η_1, η_2, and η_3.

design of these isolators. For NSIABI systems, the variation of optimal design parameters versus base mass ratio needs to be investigated. To perform that, Fig. 12 has been drawn where Fig. 12(a) shows the variation of optimal frequency ratio versus base mass ratio for different values of θ. The optimal frequency ratio of the isolator slightly increases when the base mass ratio of the NSIABI increases. However, the difference between optimal frequency ratio for lower to higher base mass ratio is minor. Therefore, all base mass ratio has extended the time period of the isolated structures. Interestingly, a lower inertial angle (i.e., $\theta = 10°$) provides a feasible frequency ratio for the isolator. In contrast, the higher inertial angles (i.e., $\theta \geq 15°$) overextended the flexibility of the isolated structure compared to the lower one. The time period of the isolated structure enlarged due to that particular reason. This scenario may damage the base floor of the isolator for over movement during vibration. Additionally, the lower base mass ratio with a higher angle provides a significantly lower frequency ratio, and the time period of the isolator has been over enlarged. It has over increased the flexibility to the base of the NSIABI, which may damage its base as well. Finally, $\theta \leq 10°$ has been considered optimal inertial angle, which provides optimal flexibility as well as sufficient load-bearing capacity to the isolated structure, respectively. Fig. 12(b) shows the variation of optimal damping ratio versus base mass ratio for different values of θ. The optimal damping ratio of the isolator decreases when the base mass ratio of the NSIABI increases. Hence, the higher base mass ratio provides optimal lower damping for the novel isolators, which is feasible and can be implemented for practical design purposes. Interestingly, a lower inertial angle (i.e., $\theta = 10°$) provides a feasible damping ratio for the isolator. In contrast, the higher inertial angles (i.e., $\theta \geq 15°$) overdamped the isolated structure compared to the lower one. The ductility of the isolator may reduce and damage the base as well. This application of higher damping is practically complicated and over cost compared to the lower one. Instead of response reduction, it may enlarge the deflection of the structure. The lower base mass ratio of NSIABI also provides higher damping, which is also not cost-effective. Apart from that, a lower base mass ratio with higher damping provides extended damping, making the isolated structure over-damped. Therefore, a higher base mass ratio with a lower angle (i.e., $\theta = 10°$) has been recommended for the optimal design of the NSIABI systems, respectively.

5. Comparison of optimal parameters obtained from H_2 and H_∞ optimization

Using the newly derived closed-form expressions for optimal design parameters through H_2 and H_∞ optimization method, the variation of optimal frequency ratio and the variation of optimal damping ratio versus the base mass ratio of NSIABI have been displayed in Fig. 13. In previous sections, it has already been shown that for lower angle (i.e., $\theta \leq 30°$), the effective mass of novel isolators has amplified the most. In fact, the most feasible design for each isolator has been achieved at lower angles which provides optimal vibration reduction capacity for each isolator. To keep it in mind, for Fig. 13, θ has been considered as 10° and other design parameters have been considered as $\eta_a = 2$, and $\mu_T = 0.10$. The significant differences for H_2 and H_∞ optimized design parameters such as frequency and damping ratio of novel isolators have been observed from Fig. 13. This scenario happens because the H_2 optimization method employs to minimize the mean squared displacement of the main structure under random excitation. In contrast, the H_∞ optimization method has been employed to minimize the maximum amplitude of the frequency response under harmonic excitation, respectively. For better visualization, the values of optimal frequency and damping ratios for each isolator have been listed in Table 2. For Table 2, the structural parameters have been considered as $\mu_{ib} = 0.70$, $\eta_a = 2$, and $\mu_T = 0.10$. Fig. 13(a) shows that the H_∞ optimized frequency ratio of novel isolators increases while H_2 optimized frequency ratios decrease with an increase in the base mass ratio of NSIABI. In fact, for NSIABI system, at higher mass ratio (i.e., $\mu_{ib} = 0.70$), the difference between optimal frequency ratios is near about 25.18% where at lower mass ratios (i.e., $\mu_{ib} = 0.20$) that is 13%. These trends have also been observed for NSBI and IABI systems, respectively. Therefore, the higher base mass ratio has lengthened the time period of the H_2 optimized isolated structures more than the lower base mass ratio while this trend is reciprocal for H_∞ optimized isolated structures. However, the variation of H_∞ optimized frequency ratio for lower to higher base mass ratio is minor. Overall, the higher base mass ratio has lengthened the time period of the isolated structures more than the lower base mass ratio. However, the nature of the optimal damping ratio plots is different from the optimal frequency ratio plots. Fig. 13(b) shows that both H_2 and H_∞ optimized damping ratio of the novel isolators decrease with increases of the base mass ratio of NSIABI. The trend of values is also different from Fig. 13(a). Hence, for NSIABI system, at higher mass ratio (i.e., $\mu_{ib} = 0.70$), the difference between optimal damping ratios is near about 5.67% where at lower mass ratios (i.e., $\mu_{ib} = 0.20$) that is 19.17%. NSBI and IABI, respectively, have followed the same trends. Therefore, the higher base mass ratio has provided lower damping for the novel isolators, which is feasible and can also be implemented for practical design purposes. The lower damping system is also cost-effective and more durable than the higher damping. The lower base mass ratio of NSIABI has provided higher damping, which is also feasible but not cost-effective. The durability of the isolated structure has also been distressed due to the higher damping. Therefore, choosing a little higher base mass ratio is recommended for the optimal design of these novel isolators, feasible, cost-effective, and more durable.

Now, the variation of structural displacement of each H_2 and H_∞ optimized isolated structure has been investigated. To perform that, the variation of displacement of the main structure of each isolated structure versus frequency ratio has been shown in Fig. 14. Table 2 has been employed to plot Fig. 14. The viscous damping ratio of the

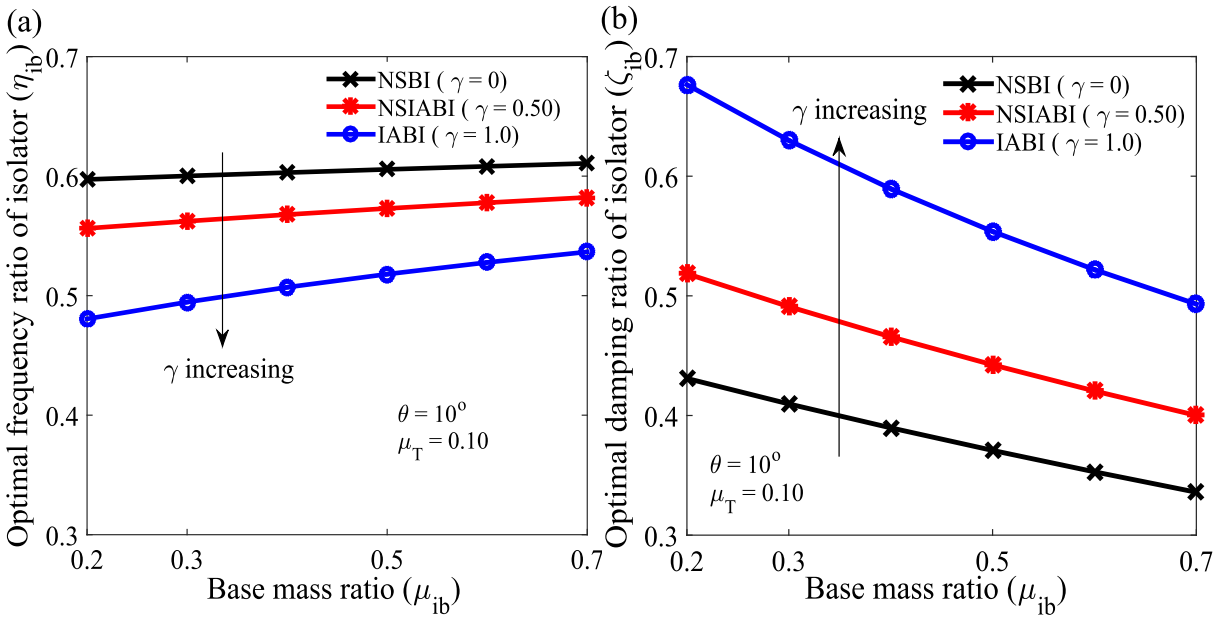

Fig. 11. (a) The variations of optimal frequency ratio η_{ib} versus base mass ratio μ_{ib} of the novel isolators have been plotted for different values of mass tuning ratio γ. (b) The variations of optimal damping ratio ζ_{ib} versus base mass ratio μ_{ib} of the novel isolators have been plotted for different values of mass tuning ratio γ. For both graphs, the black ($\gamma = 0$), red ($\gamma = 0.5$), and blue ($\gamma = 1.0$) lines with markers have been employed to indicate these plots for each isolator (i.e., NSBI, NSIABI, IABI). Other system parameters are considered as $\mu_T = 0.10$ and $\theta = 10°$.

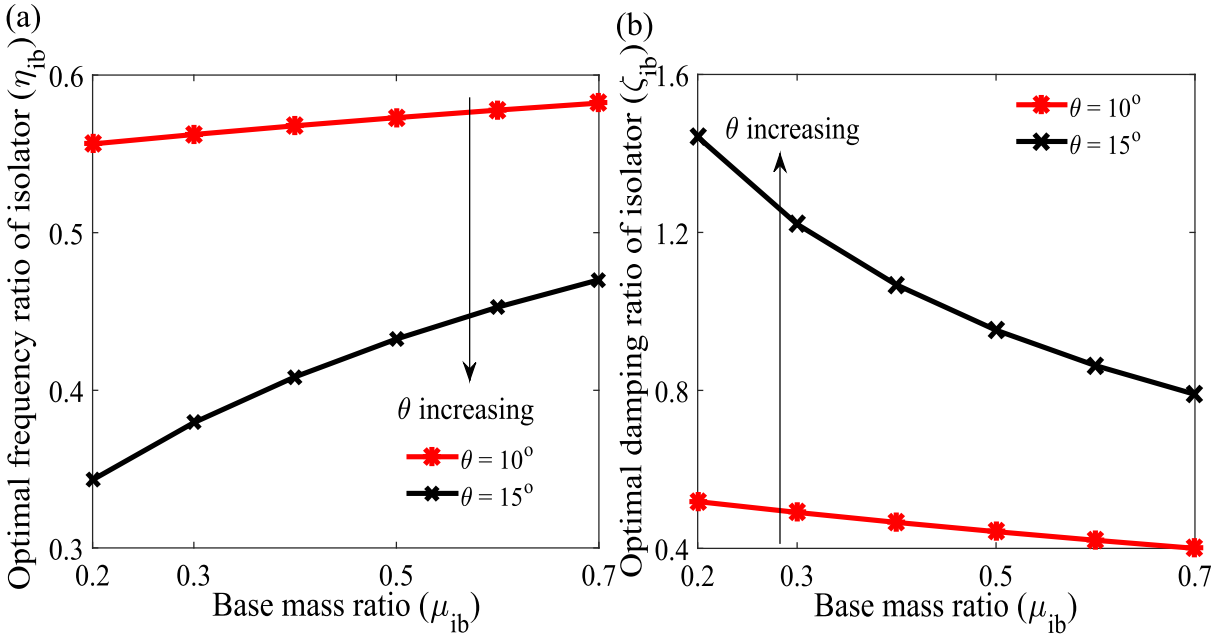

Fig. 12. (a) The variations of optimal frequency ratio η_{ib} versus base mass ratio μ_{ib} of the NSIABI system have been plotted for different values of inertial angle θ. (b) The variations of optimal damping ratio ζ_{ib} versus base mass ratio μ_{ib} of the NSIABI system have been plotted for different values of inertial angle θ. For both graphs, the red ($\theta = 10°$) and black ($\theta = 15°$) lines with markers have been employed to indicate each plot. Other system parameters are considered as $\mu_T = 0.10$ and $\gamma = 0.50$.

Table 2
Exact values of optimal design parameters.

Optimal parameters	NSBI		NSIABI ($\gamma = 0.50$)		IABI	
	H_2	H_∞	H_2	H_∞	H_2	H_∞
Frequency ratio of isolators (η_{ib})	0.4144	0.6107	0.4356	0.5822	0.4605	0.5366
Damping ratio of isolators (ζ_{ib})	0.3589	0.3359	0.3773	0.4	0.3988	0.4931

structure ζ_s is considered as 0.01. Fig. 14(a) shows the displacement of the main structure isolated by H_2 and H_∞ optimized NSBI systems, respectively. The peak displacement of H_2 and H_∞ optimized structure has been obtained as 2.4636 and 2.7674. Therefore, the difference between peak values is determined as 10.97% while for H_2 and H_∞ optimized NSIABI systems; the difference is 7.16%. The peaks values for

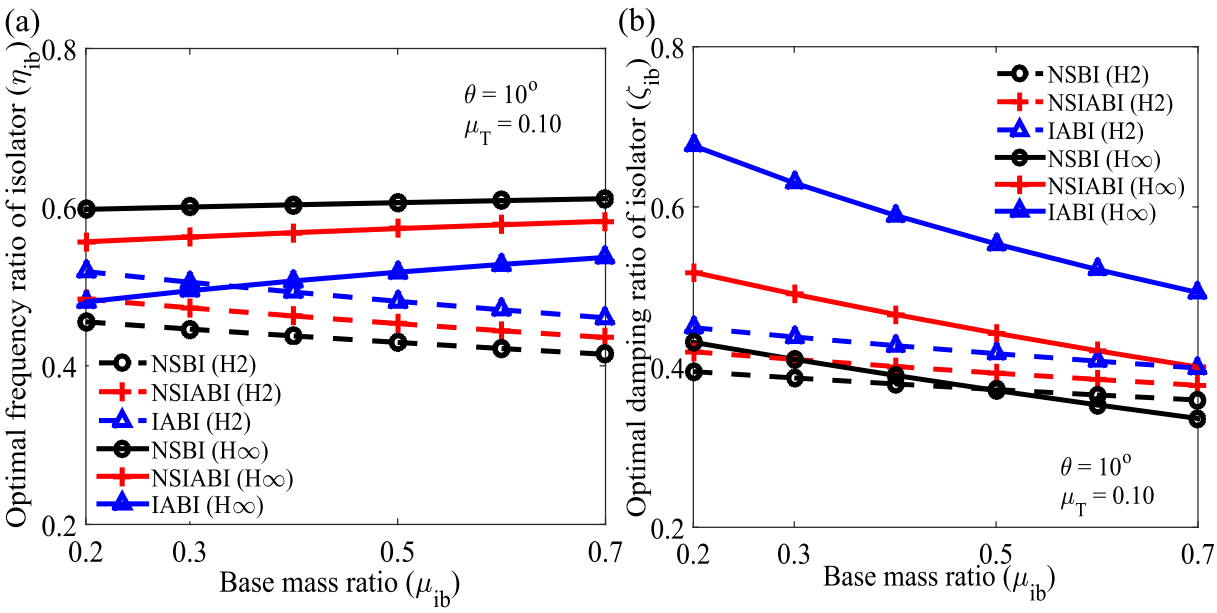

Fig. 13. (a) The variations of optimal frequency ratio η_{ib} versus base mass ratio μ_{ib} of the H_2 and H_∞ optimized novel isolators have been plotted for different values of mass tuning ratio γ. (b) The variations of optimal damping ratio ζ_{ib} versus base mass ratio μ_{ib} of the H_2 and H_∞ optimized novel isolators have been plotted for different values of mass tuning ratio γ. For both graphs, the black ($\gamma = 0$), red ($\gamma = 0.5$), and blue ($\gamma = 1.0$) lines with markers have been employed to indicate these plots for each isolator (i.e., NSBI, NSIABI, IABI). Other system parameters are considered as $\mu_T = 0.10$ and $\theta = 10°$.

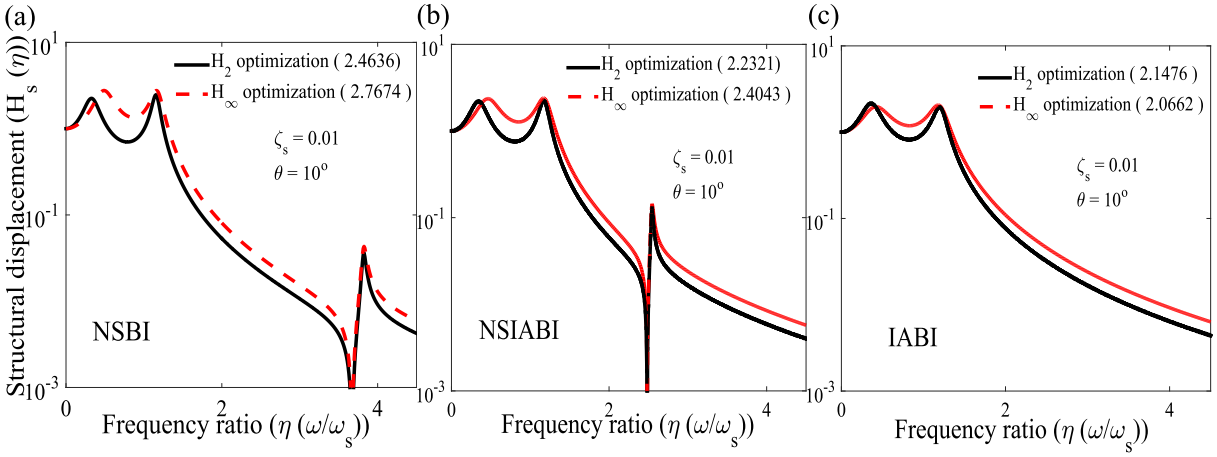

Fig. 14. The variations of displacement of the main structure $H_s(\eta)$ isolated by (a) NSBI ($\gamma = 0$), (b) NSIABI ($\gamma = 0.50$), and (c) IABI ($\gamma = 1.0$) versus frequency ratio $\eta(\omega/\omega_s)$ have been plotted for H_2 and H_∞ optimized design parameters. Eqs. (A.6) and (A.7) have been applied to obtain the optimal frequency and damping ratio of the H_2 optimized novel isolators, which have been applied to plot these graphs. Eqs. (73), (75) and (76) have been applied to obtain the optimal frequency and damping ratio of the H_∞ optimized novel isolators, which have been applied to plot these graphs. The black and red dash lines have been implemented to address the displacement plot of the main structures isolated by H_2 and H_∞ novel isolators. Other system parameters are considered as $\zeta_s = 0.01$, $\mu_{ib} = 0.70$ and $\theta = 10°$.

NSIABI optimized systems have already shown in Fig. 14(b). However, for IABI systems, this scenario is reciprocal. Fig. 14(c) shows that the peak values of the main structure isolated by H_2 and H_∞ optimized IABI systems have been determined as 2.1476 and 2.0662, respectively. Therefore, the structural displacement of H_2 optimized IABI system 3.8% more than the H_∞ optimized IABI system, respectively. These numerical values indicate that H_2 optimized NSBI and NSIABI systems are more effective than H_∞ optimized NSBI and NSIABI system while H_∞ optimized IABI is more effective than H_2 optimized IABI system, respectively. However, the variation is less for each optimized system (i.e., $< 11\%$). Overall both optimized novel isolators are more feasible, cost-effective, and durable than the traditional base isolators.

6. Performance evaluation of optimized novel base isolators

After deriving the exact closed-form expressions for optimal design parameters for novel base isolation devices using H_2 and H_∞ optimization methods, the optimal performance of each isolator has been determined. The peak displacement amplitude of main structures isolated by each isolator has been obtained and compared with the structure's corresponding displacement response isolated by the traditional base isolator. These evaluation processes have helped to investigate the exact vibration reduction capacity of each novel isolator compared to the traditional one. First, the dynamic performance of H_2 optimized NSBI, NSIABI, and IABI systems have been investigated and later the H_∞ one. Therefore, the variation of structural displacements of controlled and uncontrolled structures versus frequency ratio has been shown in Fig. 15(a). To plot this figure, Eq. (A.6) and Eq. (A.7) have been utilized to obtain the optimal design parameters and other system

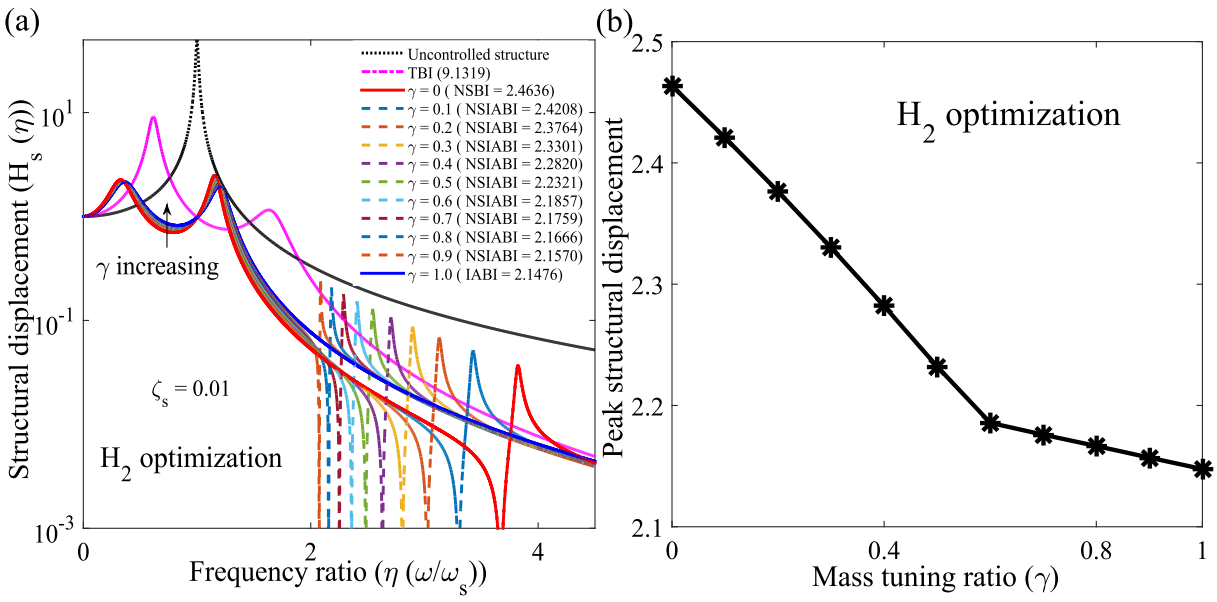

Fig. 15. (a) The variations of displacement of the main structure $H_s(\eta)$ isolated by TBI, NSBI ($\gamma = 0$), (b) NSIABI ($0.10 < \gamma < 0.90$), and IABI ($\gamma = 1.0$) versus frequency ratio $\eta(\omega/\omega_s)$ have been plotted for different values of mass tuning ratio of the novel isolators. The black dotted and magenta dash-dotted, red, blue, other colored dash–dash lines have been applied to indicate the displacement of the uncontrolled structure and structure isolated by TBI, NSBI, IABI, and NSIABI systems. Eqs. (A.6) and (A.7) have been applied to obtain the optimal frequency and damping ratio of the H_2 optimized novel isolators, which have been applied to draw this graph. Other system parameters are considered as $\zeta_s = 0.01$, $\mu_{ib} = 0.70$ and $\theta = 10°$. (b) The variation of peak structural displacement versus mass tuning ratio γ of the novel isolators has been drawn. The black line with marker employs to indicate this plot.

parameters are considered as $\mu_{ib} = 0.7$, $\zeta_s = 0.01$, $\theta = 10°$, $\eta_a = 2$, and $\mu_T = 0.10$. Using Eq. (A.6) and for $\gamma = 0, 0.1, 0.2, \ldots, 1$, the optimal frequency ratios of the novel isolators η_{ib} have been determined as 0.4144, 0.4184, 0.4226, 0.4268, 0.4311, 0.4356, 0.4403, 0.4451, 0.45, 0.4552, 0.4605. The optimal damping ratio ζ_{ib} have been obtained as 0.3589, 0.3624, 0.3659, 0.3696, 0.3734, 0.3773, 0.3813, 0.3855, 0.3897, 0.3942, 0.3988 using Eq. (A.7). After considering these parameters, the peak displacement amplitudes of main structures isolated by novel isolators have been determined as 2.4636, 2.4208, 2.3764, 2.3301, 2.2820, 2.2321, 2.1857, 2.1759, 2.1666, 2.1570, 2.1476, while the peak displacement amplitude of the structure isolated by TBI has been evaluated as 9.1319. Therefore, these results indicate that the vibration reduction capacity of NSBI, NSIABI, and IABI is significantly 73.02%, 75.55%, and 76.48%, superior to the TBI. For better visualizing these results, the variation of peak displacement amplitude of the main structure versus the mass tuning ratio of NSIABI systems has been displayed in Fig. 15(b). After that, the performance evaluation of H_∞ optimized novel isolators has proceeded. Therefore, the variation of structural displacements of controlled and uncontrolled structures versus frequency ratio has been shown in Fig. 16(a). For these plots, the optimal design parameters such as frequency and damping ratio of NSIABI systems have been determined using Eq. (73), Eq. (75), and Eq. (76). Other design parameters are considered as $\mu_{ib} = 0.7$, $\zeta_s = 0.01$, $\theta = 10°$, $\eta_a = 2$, and $\mu_T = 0.10$. Using Eq. (73) and for $\gamma = 0, 0.1, 0.2, \ldots, 1$, the optimal frequency ratios of the novel isolators η_{ib} have been determined as 0.6106, 0.6058, 0.6006, 0.5949, 0.5888, 0.5822, 0.5749, 0.5668, 0.5579, 0.5479, 0.5366. The optimal damping ratio ζ_{ib} have been obtained as 0.3358, 0.3474, 0.3595, 0.3722, 0.3857, 0.4, 0.4154, 0.4320, 0.4502, 0.4704, 0.4930 using Eq. (75), and Eq. (76), respectively. All the optimal design parameters for each isolator have been considered for these plots. It needs to be noted that for TBI, μ_T in Eq. (11) is considered as 0, and the NSIABI system will behave as TBI. After considering these parameters, the peak displacement amplitudes of main structures isolated by novel isolators have been determined as 2.7675, 2.6896, 2.6166, 2.5448, 2.4741, 2.4043, 2.3354, 2.2672, 2.1997, 2.1327, 2.0662, while the maximum displacement amplitude of structure isolated by TBI has been obtained as 9.1319. Hence, results show that the vibration reduction capacity of NSBI, NSIABI, and IABI is significantly 69.69%, 73.67%, and 77.37% superior to the TBI, respectively. For better visualizing these results, the variation of peak displacement amplitude of the main structure versus the mass tuning ratio of NSIABI systems has been shown in Fig. 16(b). For both cases, it has been observed that the IABI system has superior vibration reduction capacity to the NSBI and NSIABI. This scenario happens because the inertial amplifier has been enhanced the effective mass of the isolator, which amplifies the inertial forces inside the isolated structure during vibration. In contrast, the negative stiffness only provides additional flexibility to the isolated structure, enhancing the main structure's time period during vibration. However, the combined effect of the inertial amplifier and negative stiffness is robust. As the vibration reduction capacity of H_2 and H_∞ optimized IABI is only 0.46% and 3% superior to the H_2 and H_∞ optimized NSIABI system, which is very much negligible. The best part of this paper is that all three novel base isolators have at least 69% more vibration reduction capacity than traditional base isolators, respectively.

7. Summary and conclusions

Inspired by the negative stiffness and inertial amplifier concept, this paper proposed a negative stiffness inertial-amplifier-base-isolator (NSIABI). From this NSIABI, there are two different novel isolators: negative stiffness base isolator (NSBI) and inertial amplifier base isolator (IABI) produced by altering the novel isolators' mass tuning ratio combined static mass of the entire system constant. These novel isolators have been significantly increased the dynamic effective mass of the system, simultaneously enhancing the time period of the controlled structure during vibration. Therefore, these improved the vibration reduction capacity of the traditional base isolator without increasing the total static masses. To drive the closed-form expressions for optimal design parameters, H_2 and H_∞ optimization methods have been employed when the controlled structures were subjected to white-noise random and harmonic excitations, respectively. Finally, the responses of H_2 and H_∞ optimized base isolators have been determined and compared

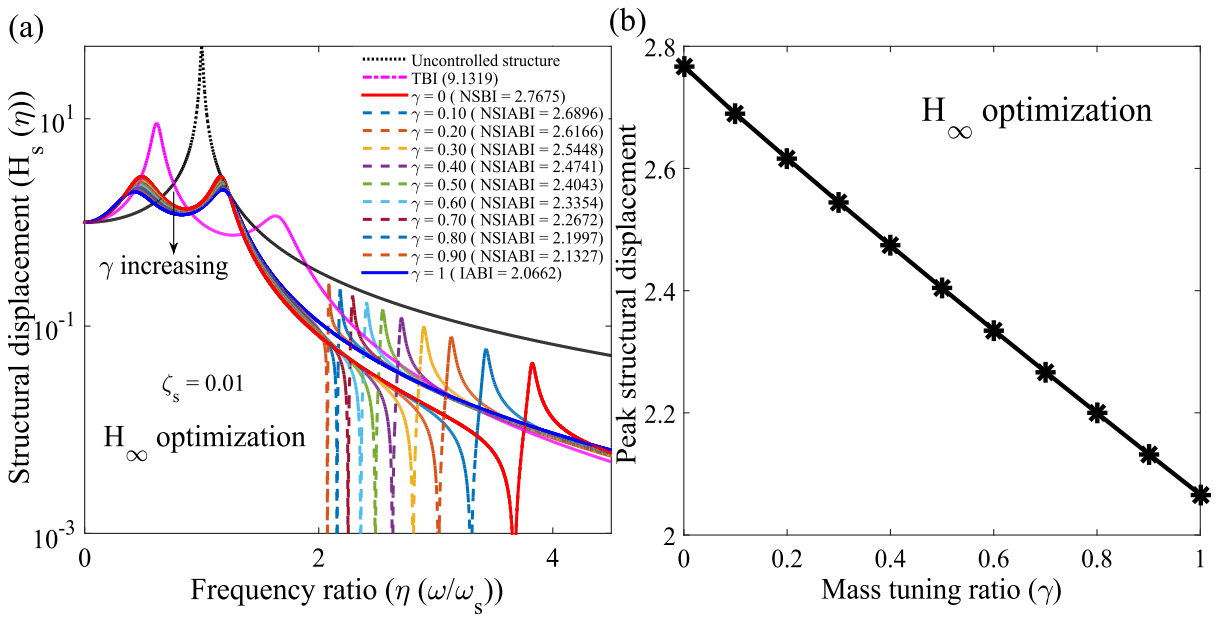

Fig. 16. (a) The variations of displacement of the main structure $H_s(\eta)$ isolated by TBI, NSBI ($\gamma = 0$), (b) NSIABI ($0.10 < \gamma < 0.90$), and IABI ($\gamma = 1.0$) versus frequency ratio $\eta(\omega/\omega_s)$ have been plotted for different values of mass tuning ratio of the novel isolators. The black dotted and magenta dash-dotted, red, blue, other colored dash–dash lines have been applied to indicate the displacement of the uncontrolled structure and structure isolated by TBI, NSBI, IABI, and NSIABI systems. Eqs. (73), (75) and (76) have been applied to obtain the optimal frequency and damping ratio of the H_∞ optimized novel isolators, which have been applied to draw this graph. Other system parameters are considered as $\zeta_s = 0.01$, $\mu_{ib} = 0.70$ and $\theta = 10°$. (b) The variation of peak structural displacement versus mass tuning ratio γ of the novel isolators has been drawn. The black line with marker employs to indicate this plot.

to investigate the vibration reduction capacity of each novel isolator compared to the traditional base isolator. The significant outcomes are the following:

- The newly derived exact closed-form expressions for optimal design parameters of three novel isolators, namely NSBI, NSIABI, and IABI, have been introduced in this paper. These expressions have been derived analytically using H_2 and H_∞ optimization methods, respectively.
- Results showed that the vibration reduction capacity of H_2 optimized NSBI, NSIABI, and IABI is significantly 73.02%, 75.55%, and 76.48%, superior to the TBI, respectively.
- While, the vibration reduction capacity of H_∞ optimized NSBI, NSIABI, and IABI is significantly 69.69%, 73.67%, and 77.37% superior to the TBI, respectively.
- Results from both optimized systems showed that the IABI system had more vibration reduction capacity than NSBI and NSIABI. This scenario happens because the inertial amplifier has been enhanced the effective mass of the traditional base isolator, which amplifies the inertial forces inside the isolated structure during vibration.
- The effective mass amplification occurred at $\theta \leq 30°$, which have been recognized as the critical angles for the novel isolators, respectively. Besides, the significant amount of mass amplification occurred at $\theta \leq 12°$.
- The dynamic negative effective stiffness provided additional flexibility to the isolated structure, enhancing the main structure's time period during vibration. Additionally, the dynamic effective stiffness amplifications at $0.65 \leq \eta/\eta_a \leq 1.0$ and $2 \leq \eta/\eta_a \leq 3.0$ also provides sufficient load-bearing capacity to the controlled structures during vibration simultaneously.
- Overall, NSBI ($\gamma = 0$) and NSIABI ($0.1 \leq \gamma \leq 0.5$) produce a significant amount of dynamic negative effective stiffness amplification. In contrast, a significant amount of dynamic positive effective mass amplification has been observed in IABI ($\gamma = 1$) and other NSIABI systems having the values of $0.6 \leq \gamma \leq 0.9$. Therefore, the combination of the negative stiffness and inertial amplifier is robust. The NSIABI systems can enhance the structure's time period and increase the energy dissipation property of the base isolator simultaneously during vibration.
- For all cases, the IABI system ($\gamma = 1.0$) does not produce any negative mass and negative stiffness during vibration. It can only provide a significant amount of dynamic positive effective mass, which have amplified the effective damping of the system. Hence, the energy dissipation capacity of the isolator has been increased during vibration, respectively.
- Finally, it has been concluded that these negative stiffness inertial amplifiers based isolators have enhanced the energy dissipation capacity of the traditional base isolators, providing additional flexibility simultaneously sufficient load-bearing capacity to the controlled structures.
- Another observation is that the vibration reduction capacity of both optimized IABI is only 0.46% and 3% superior to the H_2 and H_∞ optimized NSIABI system, which is very much negligible. Overall these three novel base isolators have at least 69% more vibration reduction capacity than traditional base isolators, respectively.

One of the main contributions of this paper is the new closed-form expressions for optimal design parameters of novel isolators. These expressions provided optimal design for these novel isolators, which helped to achieve maximum vibration reduction. These novel isolators are cost-effective and have better energy dissipation than other existing base isolators without damaging the primary structure. The practical realization, experimentation, and prototyping of the proposed negative stiffness inertial amplifier base isolator will be the future scope of the research.

CRediT authorship contribution statement

S. Chowdhury: Methodology, Software, Data curation, Writing – original draft, Visualization, Investigation. **A. Banerjee:** Conceptualization, Visualization, Investigation, Supervision, Securing the fund, Reviewing & editing, Critical discussion. **S. Adhikari:** Conceptualization, Supervision, Reviewing & editing.

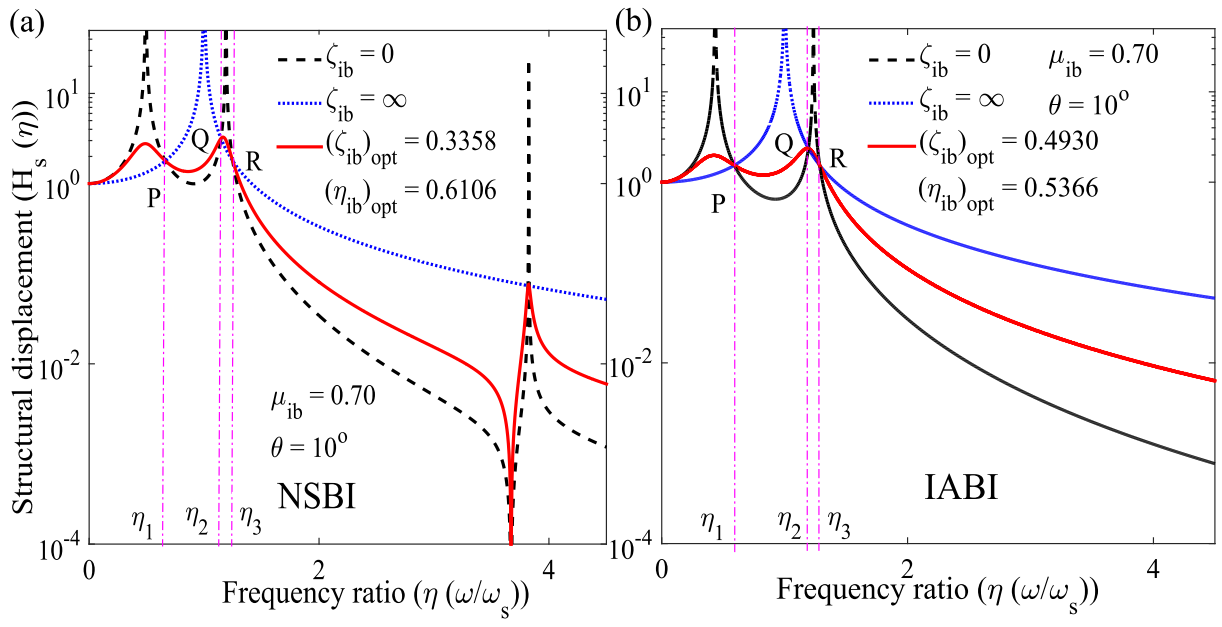

Fig. C.17. The variations of displacement of the main structure $H_s(\eta)$ isolated by (a) NSBI ($\gamma = 0$) and (b) IABI ($\gamma = 1$) versus frequency ratio $\eta(\omega/\omega_s)$ have been plotted for different values of damping ratio of these novel isolators. The black dash, blue dotted, and red lines have been implemented to address the displacement plots for damping ratio of 0, ∞, and $(\zeta_{ib})_{opt}$. Eqs. (73), (75) and (76) have been applied to obtain the optimal frequency and damping ratio of the NSBI and IABI systems, which have been applied to plot these graphs. Other system parameters are considered as $\mu_{ib} = 0.70$ and $\theta = 10°$. For all graphs, P, Q, and R are indicating three fixed points, and the corresponding frequency ratios have been denoted as η_1, η_2, and η_3.

Declaration of competing interest

The authors declare that they have no known competing financial interests or personal relationships that could have appeared to influence the work reported in this paper.

Acknowledgment

The authors' would like to acknowledge the Inspire faculty grant, grant number DST/INSPIRE/04/2018/000052, for partial financial support for the project.

Appendix A. Closed-form expressions from H_2 optimization method

In Eq. (42), $q = i\omega$ and coefficients of q have been listed below.

$$
\begin{aligned}
a_0 &= \mu_\vartheta \omega_a{}^2 \omega_{ib}{}^2 \omega_s{}^2 \\
a_1 &= 2\,\zeta_{ib}\mu_\vartheta \omega_a{}^2 \omega_{ib} \omega_s{}^2 + 2\,\zeta_s \mu_\vartheta \omega_a{}^2 \omega_{ib}{}^2 \omega_s \\
a_2 &= 4\,\zeta_{ib}\zeta_s \mu_\vartheta \omega_a{}^2 \omega_{ib} \omega_s + \mu_{\Phi} \omega_{ib}{}^2 \omega_s{}^2 + \mu_\vartheta \omega_a{}^2 \omega_{ib}{}^2 \\
&\quad + \mu_\vartheta \omega_a{}^2 \omega_s{}^2 + \omega_a{}^2 \omega_s{}^2 \\
a_3 &= 2\,\zeta_{ib}\mu_{\Phi} \omega_{ib} \omega_s{}^2 + 2\,\zeta_{ib}\mu_\vartheta \omega_a{}^2 \omega_{ib} + 2\,\zeta_s \mu_{\Phi} \omega_{ib}{}^2 \omega_s \\
&\quad + 2\,\zeta_s \mu_\vartheta \omega_a{}^2 \omega_s + 2\,\zeta_s \omega_a{}^2 \omega_s \\
a_4 &= 4\,\zeta_{ib}\zeta_s \mu_{\Phi} \omega_{ib} \omega_s + \mu_{\Phi} \omega_{ib}{}^2 + \mu_{\Phi} \omega_s{}^2 + \mu_\vartheta \omega_a{}^2 + \omega_s{}^2 \\
a_5 &= 2\,\zeta_{ib}\mu_{\Phi} \omega_{ib} + 2\,\zeta_s \mu_{\Phi} \omega_s + 2\,\zeta_s \omega_s \\
a_6 &= \mu_{\Phi}
\end{aligned}
\tag{A.1}
$$

The values of b_n in Eq. (43) have been obtained from Eq. (45). Therefore, the values of b_n have been derived as

$$
\begin{aligned}
&n = 6, b_0 = \mu_\vartheta{}^2 \omega_a{}^4 \omega_{ib}{}^4, b_1 = 4\,\zeta_{ib}{}^2 \mu_\vartheta{}^2 \omega_a{}^4 \omega_{ib}{}^2 - 2\,\mu_{\Phi}\mu_\vartheta \omega_a{}^2 \omega_{ib}{}^4, \\
&b_2 = -8\,\zeta_{ib}{}^2 \mu_{\Phi}\mu_\vartheta \omega_a{}^2 \omega_{ib}{}^2 + \mu_{\Phi}{}^2 \omega_{ib}{}^4, \\
&b_3 = 4\,\zeta_{ib}{}^2 \mu_{\Phi}{}^2 \omega_{ib}{}^2, b_4 = 0, \quad \text{and} \quad b_5 = 0
\end{aligned}
\tag{A.2}
$$

The extended form of the Eq. (46) has been listed below.

$$
\sigma_{y_s}^2 = \frac{S_0 \pi\, \eta_{ib} \left(\left(4\,\zeta_{ib}{}^2 \mu_\vartheta + \mu_\vartheta \eta_{ib}{}^2 + 1 \right) \eta_a{}^2 - 4\,\zeta_{ib}{}^2 \mu_{\Phi} - \mu_{\Phi} \eta_{ib}{}^2 - 1 \right)}{2\zeta_{ib} \left(\eta_a{}^2 - 1 \right) \omega_s{}^3}
\tag{A.3}
$$

The extended form of the Eq. (47) has been listed below.

$$
\sigma_{\dot{y}_s}^2 = \frac{S_0 \pi \omega_{ib} \left(\begin{array}{c} \left(4\,\zeta_{ib}{}^2 \mu_\vartheta + 4\,\zeta_{ib}{}^2 + \mu_\vartheta \eta_{ib}{}^2 \right) \eta_a{}^2 \\ -4\,\zeta_{ib}{}^2 \mu_{\Phi} - 4\,\zeta_{ib}{}^2 - \mu_{\Phi} \eta_{ib}{}^2 \end{array} \right)}{2\zeta_{ib} \left(\eta_a{}^2 - 1 \right)}
\tag{A.4}
$$

The extended form of the Eq. (48) has been listed below.

$$
\sigma_{sf}^2 = \frac{S_0 \pi\, \omega_{ib} \left(\left(4\,\zeta_{ib}{}^2 \mu_\vartheta + \mu_\vartheta \eta_{ib}{}^2 + 1 \right) \eta_a{}^2 - 4\,\zeta_{ib}{}^2 \mu_{\Phi} - \mu_{\Phi} \eta_{ib}{}^2 - 1 \right)}{2\zeta_{ib} \left(\eta_a{}^2 - 1 \right)}
\tag{A.5}
$$

The non-dimensional form of Eq. (52) has been expressed as

$$
(\eta_{ib})_{opt} = \frac{\sqrt{2} \sqrt{(\mu_\vartheta \eta_a{}^2 - \mu_{\Phi}) \left(\eta_a{}^2 - 1 \right)}}{2(\mu_\vartheta \eta_a{}^2 - \mu_{\Phi})}
\tag{A.6}
$$

The non-dimensional form of Eq. (53) has been expressed as

$$
(\zeta_{ib})_{opt} = 1/4 \sqrt{\frac{6\,\eta_a{}^2 - 6}{\mu_\vartheta \eta_a{}^2 - \mu_{\Phi}}}
\tag{A.7}
$$

Appendix B. Closed-form expressions from H_∞ optimization method

The coefficients of x in Eq. (71) have been listed below and using these expressions, the closed-form expressions for optimal frequency

ratio of the novel isolators have been derived.

$$
\begin{aligned}
w_2 &= \left(-4\,{\eta_a}^2\mu_\Phi\mu_\vartheta + 4\,{\mu_\Phi}^2\right)\\
w_1 &= \left(-2\,{\eta_a}^4{\mu_\vartheta}^2 + 8\,{\eta_a}^2\mu_\Phi\mu_\vartheta - 2\,{\eta_a}^2\mu_\Phi - 2\,{\eta_a}^2\mu_\vartheta - 6\,{\mu_\Phi}^2 + 6\,\mu_\Phi\right)\\
w_0 &= {\eta_a}^4{\mu_\vartheta}^2 - {\eta_a}^4\mu_\vartheta - 3\,{\eta_a}^2\mu_\Phi\mu_\vartheta + {\eta_a}^2\mu_\Phi + 3\,{\eta_a}^2\mu_\vartheta - {\eta_a}^2 + 2\,{\mu_\Phi}^2\\
&\quad - 4\,\mu_\Phi + 2
\end{aligned}
\tag{B.1}
$$

Appendix C. Optimal displacement plots of H_∞ optimized NSBI and IABI systems

See Fig. C.17.

References

[1] Touaillon J. Improvement in Buildings. Google Patents. U.S. Patent No. 99, 973, 1870.

[2] Ebrahimi B, Bolandhemmat H, Khamesee MB, Golnaraghi F. A hybrid electromagnetic shock absorber for active vehicle suspension systems. Veh Syst Dyn 2011;49(1–2):311–32.

[3] Du H, Li W, Zhang N. Semi-active variable stiffness vibration control of vehicle seat suspension using an MR elastomer isolator. Smart Mater Struct 2011;20(10):105003.

[4] Aly AA, Salem FA. Vehicle suspension systems control: a review. Int J Control Autom Syst 2013;2(2):46–54.

[5] Esmailzadeh E. Optimization of pneumatic vibration isolation system for vehicle suspension. 1978.

[6] Wei X, Lui H, Qin Y. Fault isolation of rail vehicle suspension systems by using similarity measure. In: Proceedings of 2011 IEEE international conference on service operations, logistics and informatics. IEEE; 2011, p. 391–6.

[7] Lindberg E, Östberg M, Hörlin N-E, Göransson P. A vibro-acoustic reduced order model using undeformed coupling interface substructuring–application to rubber bushing isolation in vehicle suspension systems. Appl Acoust 2014;78:43–50.

[8] Bai X-X, Jiang P, Qian L-J. Integrated semi-active seat suspension for both longitudinal and vertical vibration isolation. J Intell Mater Syst Struct 2017;28(8):1036–49.

[9] Malhotra PK. Method for seismic base isolation of liquid-storage tanks. J Struct Eng 1997;123(1):113–6.

[10] Malhotra PK. New method for seismic isolation of liquid-storage tanks. Earthq Eng Struct Dyn 1997;26(8):839–47.

[11] Cheng X, Jing W, Gong L. Simplified model and energy dissipation characteristics of a rectangular liquid-storage structure controlled with sliding base isolation and displacement-limiting devices. J Perform Constr Facil 2017;31(5):04017071.

[12] Abalı E, Uckan E. Parametric analysis of liquid storage tanks base isolated by curved surface sliding bearings. Soil Dyn Earthq Eng 2010;30(1–2):21–31.

[13] Liang B, Tang J-x. Vibration studies of base-isolated liquid storage tanks. Comput Struct 1994;52(5):1051–9.

[14] Das A, Deb SK, Dutta A. Shake table testing of un-reinforced brick masonry building test model isolated by U-FREI. Earthq Eng Struct Dyn 2016;45(2):253–72.

[15] Schnitzer E. Band-pass shock and vibration absorbers for application to aircraft landing gear. No. 3803. National Advisory Committee for Aeronautics; 1956.

[16] Makris N. Seismic isolation: Early history. Earthq Eng Struct Dyn 2019;48(2):269–83.

[17] Kelly JM. Base isolation: linear theory and design. Earthq Spectra 1990;6(2):223–44.

[18] Hwang J, Chiou J. An equivalent linear model of lead-rubber seismic isolation bearings. Eng Struct 1996;18(7):528–36.

[19] Kazeminezhad E, Kazemi MT, Mirhosseini SM. Assessment of the vertical stiffness of elastomeric bearing due to displacement and rotation. Int J Non Linear Mech 2020;119:103306.

[20] Baduidana M, Kenfack-Jiotsa A. Optimal design of inerter-based isolators minimizing the compliance and mobility transfer function versus harmonic and random ground acceleration excitation. J Vib Control 2021;27(11–12):1297–310.

[21] Čakmak D, Tomičević Z, Wolf H, Božić Ž, Semenski D. Stability and performance of supercritical inerter-based active vibration isolation systems. J Sound Vib 2021;116234.

[22] Hu Y, Chen MZ. Performance evaluation for inerter-based dynamic vibration absorbers. Int J Mech Sci 2015;99:297–307.

[23] Sun H, Zuo L, Wang X, Peng J, Wang W. Exact H2 optimal solutions to inerter-based isolation systems for building structures. Struct Control Health Monit 2019;26(6):e2357.

[24] Cheng Z, Palermo A, Shi Z, Marzani A. Enhanced tuned mass damper using an inertial amplification mechanism. J Sound Vib 2020;115267.

[25] Chen MZ, Hu Y. Analysis for inerter-based vibration system. In: Inerter and its application in vibration control systems. Springer; 2019, p. 19–39.

[26] Asami T, Nishihara O, Baz AM. Analytical solutions to H_∞ and H_2 optimization of dynamic vibration absorbers attached to damped linear systems. J Vib Acoust 2002;124(2):284–95.

[27] Den Hartog JP. Mechanical vibrations. Courier Corporation; 1985.

[28] Cheung Y, Wong WO. H_∞ Optimization of a variant design of the dynamic vibration absorber—Revisited and new results. J Sound Vib 2011;330(16):3901–12.

[29] Allen JC. H_∞ engineering and amplifier optimization. Springer Science & Business Media; 2012.

[30] Chun S, Lee Y, Kim T-H. H_∞ Optimization of dynamic vibration absorber variant for vibration control of damped linear systems. J Sound Vib 2015;335:55–65.

[31] Hua Y, Wong W, Cheng L. Optimal design of a beam-based dynamic vibration absorber using fixed-points theory. J Sound Vib 2018;421:111–31.

[32] Palazzo B, Petti L. Optimal structural control in the frequency domain: control in norm H_∞ and H_2. J Struct Control 1999;6(2):205–21.

[33] Qian F, Luo Y, Sun H, Tai WC, Zuo L. Optimal tuned inerter dampers for performance enhancement of vibration isolation. Eng Struct 2019;198:109464.

[34] Crandall SH, Mark WD. Random vibration in mechanical systems. Academic Press; 2014.

[35] Shen Y, Peng H, Li X, Yang S. Analytically optimal parameters of dynamic vibration absorber with negative stiffness. Mech Syst Signal Process 2017;85:193–203.

[36] Smith MC. The inerter: A retrospective. Ann Rev Control Robot Auton Syst 2020;3:361–91.

[37] Smith MC. Synthesis of mechanical networks: the inerter. IEEE Trans Autom Control 2002;47(10):1648–62.

[38] Smith MC, Wang F-C. Performance benefits in passive vehicle suspensions employing inerters. Veh Syst Dyn 2004;42(4):235–57.

[39] Wang F-C, Liao M-K, Liao B-H, Su W-J, Chan H-A. The performance improvements of train suspension systems with mechanical networks employing inerters. Veh Syst Dyn 2009;47(7):805–30.

[40] Wang F-C, Yu C-H, Chang M-L, Hsu M. The performance improvements of train suspension systems with inerters. In: Proceedings of the 45th IEEE conference on decision and control. IEEE; 2006, p. 1472–7.

[41] Wang F-C, Hsieh M-R, Chen H-J. Stability and performance analysis of a full-train system with inerters. Veh Syst Dyn 2012;50(4):545–71.

[42] Hu Y, Chen MZ, Sun Y. Comfort-oriented vehicle suspension design with skyhook inerter configuration. J Sound Vib 2017;405:34–47.

[43] Chen MZ, Hu Y. Inerter and its application in vibration control systems. Springer; 2019.

[44] De Domenico D, Deastra P, Ricciardi G, Sims ND, Wagg DJ. Novel fluid inerter based tuned mass dampers for optimised structural control of base-isolated buildings. J Franklin Inst 2019;356(14):7626–49.

[45] Zhao Z, Chen Q, Zhang R, Pan C, Jiang Y. Energy dissipation mechanism of inerter systems. Int J Mech Sci 2020;184:105845.

[46] Moghimi G, Makris N. Seismic response of yielding structures equipped with inerters. Soil Dyn Earthq Eng 2020;106474.

[47] Zhao Z, Chen Q, Zhang R, Pan C, Jiang Y. Optimal design of an inerter isolation system considering the soil condition. Eng Struct 2019;196:109324.

[48] Jiang Y, Zhao Z, Zhang R, De Domenico D, Pan C. Optimal design based on analytical solution for storage tank with inerter isolation system. Soil Dyn Earthq Eng 2020;129:105924.

[49] Zhao Z, Zhang R, Wierschem NE, Jiang Y, Pan C. Displacement mitigation–oriented design and mechanism for inerter-based isolation system. J Vib Control 2020;1077546320951662.

[50] Ayad M, Karathanasopoulos N, Ganghoffer J-F, Lakiss H. Higher-gradient and micro-inertia contributions on the mechanical response of composite beam structures. Int J Eng Sci 2020;154:103318.

[51] Ayad M, Karathanasopoulos N, Reda H, Ganghoffer J-F, Lakiss H. Dispersion characteristics of periodic structural systems using higher order beam element dynamics. Math Mech Solids 2020;25(2):457–74.

[52] De Domenico D, Ricciardi G, Zhang R. Optimal design and seismic performance of tuned fluid inerter applied to structures with friction pendulum isolators. Soil Dyn Earthq Eng 2020;132:106099.

[53] Čakmak D, Tomičević Z, Wolf H, Božić Ž, Semenski D, Trapić I. Vibration fatigue study of the helical spring in the base-excited inerter-based isolation system. Eng Fail Anal 2019;103:44–56.

[54] Qian F, Luo Sr Y, Sun H, Tai WC, Zuo L. Performance enhancement of a base-isolation structure using optimal tuned inerter dampers. In: Active and passive smart structures and integrated systems XIII. Vol. 10967. International Society for Optics and Photonics; 2019, 1096715.

[55] Taflanidis AA, Giaralis A, Patsialis D. Multi-objective optimal design of inerter-based vibration absorbers for earthquake protection of multi-storey building structures. J Franklin Inst 2019;356(14):7754–84.

[56] Li L, Liang Q. Effect of inerter for seismic mitigation comparing with base isolation. Struct Control Health Monit 2019;26(10):e2409.

[57] Barone G, Iacono FL, Navarra G, Palmeri A. Closed-form stochastic response of linear building structures to spectrum-consistent seismic excitations. Soil Dyn Earthq Eng 2019;125:105724.

[58] Muscolino G, Palmeri A, Versaci C. Damping-adjusted combination rule for the response spectrum analysis of base-isolated buildings. Earthq Eng Struct Dyn 2013;42(2):163–82.

[59] Zhang R, Zhao Z, Pan C. Influence of mechanical layout of inerter systems on seismic mitigation of storage tanks. Soil Dyn Earthq Eng 2018;114:639–49.

[60] Zhang R, Zhao Z, Dai K. Seismic response mitigation of a wind turbine tower using a tuned parallel inerter mass system. Eng Struct 2019;180:29–39.

[61] Kuhnert WM, Gonçalves PJP, Ledezma-Ramirez DF, Brennan MJ. Inerter-like devices used for vibration isolation: A historical perspective. J Franklin Inst 2020.

[62] Yilmaz C, Hulbert GM, Kikuchi N. Phononic band gaps induced by inertial amplification in periodic media. Phys Rev B 2007;76(5):054309.

[63] Taniker S, Yilmaz C. Design, analysis and experimental investigation of three-dimensional structures with inertial amplification induced vibration stop bands. Int J Solids Struct 2015;72:88–97.

[64] Yilmaz C, Hulbert G. Theory of phononic gaps induced by inertial amplification in finite structures. Phys Lett A 2010;374(34):3576–84.

[65] Taniker S, Yilmaz C. Phononic gaps induced by inertial amplification in BCC and FCC lattices. Phys Lett A 2013;377(31–33):1930–6.

[66] Frandsen NM, Bilal OR, Jensen JS, Hussein MI. Inertial amplification of continuous structures: Large band gaps from small masses. J Appl Phys 2016;119(12):124902.

[67] Hou M, Wu JH, Cao S, Guan D, Zhu Y. Extremely low frequency band gaps of beam-like inertial amplification metamaterials. Modern Phys Lett B 2017;31(27):1750251.

[68] Yilmaz G, Hulbert, Kikuchi N. Phononic band gaps induced by inertial amplification in periodic media. Phys Rev B 2007;76:054309.

[69] Miniaci M, Mazzotti M, Amendola A, Fraternali F. Inducing dispersion curves with negative group velocity in inertially amplified phononic crystals through the application of an external state of prestress. In: XI international conference on structural dynamic. 2020, p. 612–20.

[70] Sun F, Dai X, Liu Y, Xiao L. Seismic mitigation performance of periodic foundations with inertial amplification mechanism considering superstructure-foundation interaction. Smart Mater Struct 2021;30(2):025018.

[71] Yuksel O, Yilmaz C. Shape optimization of phononic band gap structures incorporating inertial amplification mechanisms. J Sound Vib 2015;355:232–45.

[72] Taniker S, Yilmaz C. Generating ultra wide vibration stop bands by a novel inertial amplification mechanism topology with flexure hinges. Int J Solids Struct 2017;106:129–38.

[73] Barys M, Zalewski R. Analysis of inertial amplification mechanism with smart spring-damper for attenuation of beam vibrations. In: MATEC web of conferences. Vol. 157. EDP Sciences; 2018, p. 03002.

[74] Yilmaz C, Hulbert GM. Dynamics of locally resonant and inertially amplified lattice materials. In: Phani A, Hussein M, editors. Dynamics of lattice materials. 2017, p. 233.

[75] Zhou J, Dou L, Wang K, Xu D, Ouyang H. A nonlinear resonator with inertial amplification for very low-frequency flexural wave attenuations in beams. Nonlinear Dynam 2019;96(1):647–65.

[76] Barys M, Jensen JS, Frandsen NM. Efficient attenuation of beam vibrations by inertial amplification. Eur J Mech A/Solids 2018;71:245–57.

[77] Muhammad S, Wang S, Li F, Zhang C. Bandgap enhancement of periodic nonuniform metamaterial beams with inertial amplification mechanisms. J Vib Control 2020;1077546319895630.

[78] Karathanasopoulos N, Dos Reis F, Diamantopoulou M, Ganghoffer J-F. Mechanics of beams made from chiral metamaterials: Tuning deflections through normal-shear strain couplings. Mater Des 2020;189:108520.

[79] Ayad M, Karathanasopoulos N, Reda H, Ganghoffer J-F, Lakiss H. On the role of second gradient constitutive parameters in the static and dynamic analysis of heterogeneous media with micro-inertia effects. Int J Solids Struct 2020;190:58–75.

[80] Carrella A, Brennan M, Waters T. Static analysis of a passive vibration isolator with quasi-zero-stiffness characteristic. J Sound Vib 2007;301(3–5):678–89.

[81] Carrella A, Brennan M, Kovacic I, Waters T. On the force transmissibility of a vibration isolator with quasi-zero-stiffness. J Sound Vib 2009;322(4–5):707–17.

[82] Hao Z, Cao Q. The isolation characteristics of an archetypal dynamical model with stable-quasi-zero-stiffness. J Sound Vib 2015;340:61–79.

[83] Robertson WS, Kidner M, Cazzolato BS, Zander AC. Theoretical design parameters for a quasi-zero stiffness magnetic spring for vibration isolation. J Sound Vib 2009;326(1–2):88–103.

[84] Cheng C, Li S, Wang Y, Jiang X. On the analysis of a high-static-low-dynamic stiffness vibration isolator with time-delayed cubic displacement feedback. J Sound Vib 2016;378:76–91.

[85] Zheng Y, Zhang X, Luo Y, Yan B, Ma C. Design and experiment of a high-static–low-dynamic stiffness isolator using a negative stiffness magnetic spring. J Sound Vib 2016;360:31–52.

[86] Huang X, Liu X, Sun J, Zhang Z, Hua H. Vibration isolation characteristics of a nonlinear isolator using Euler buckled beam as negative stiffness corrector: a theoretical and experimental study. J Sound Vib 2014;333(4):1132–48.

[87] Fulcher BA, Shahan DW, Haberman MR, Conner Seepersad C, Wilson PS. Analytical and experimental investigation of buckled beams as negative stiffness elements for passive vibration and shock isolation systems. J Vib Acoust 2014;136(3).

[88] Liu X, Huang X, Hua H. On the characteristics of a quasi-zero stiffness isolator using Euler buckled beam as negative stiffness corrector. J Sound Vib 2013;332(14):3359–76.

[89] Winterflood J, Blair DG, Slagmolen B. High performance vibration isolation using springs in Euler column buckling mode. Phys Lett A 2002;300(2–3):122–30.

[90] Iemura H, Pradono MH. Advances in the development of pseudo-negative-stiffness dampers for seismic response control. Struct Control Health Monit Official J Int Assoc Struct Control Monit Eur Assoc Control Struct 2009;16(7–8):784–99.

[91] Iemura H, Igarashi A, Pradono MH, Kalantari A. Negative stiffness friction damping for seismically isolated structures. Struct Control Health Monit Official J Int Assoc Struct Control Monit Eur Assoc Control Struct 2006;13(2–3):775–91.

[92] Lakes RS, Lee T, Bersie A, Wang Y-C. Extreme damping in composite materials with negative-stiffness inclusions. Nature 2001;410(6828):565–7.

[93] Shi X, Zhu S. Simulation and optimization of magnetic negative stiffness dampers. Sensors Actuators A Phys 2017;259:14–33.

[94] Wu W, Chen X, Shan Y. Analysis and experiment of a vibration isolator using a novel magnetic spring with negative stiffness. J Sound Vib 2014;333(13):2958–70.

[95] Banerjee A, Das R, Calius EP. Waves in structured mediums or metamaterials: a review. Arch Comput Methods Eng 2019;26(4):1029–58.

[96] Huang H, Sun C. Theoretical investigation of the behavior of an acoustic metamaterial with extreme Young's modulus. J Mech Phys Solids 2011;59(10):2070–81.

[97] Cimellaro GP, Domaneschi M, Warn G. Three-dimensional base isolation using vertical negative stiffness devices. J Earthq Eng 2020;24(12):2004–32.

[98] Li H, Li Y, Li J. Negative stiffness devices for vibration isolation applications: A review. Adv Struct Eng 2020;23(8):1739–55.

[99] Le TD, Ahn KK. A vibration isolation system in low frequency excitation region using negative stiffness structure for vehicle seat. J Sound Vib 2011;330(26):6311–35.

[100] Xiang S, Songye Z. A comparative study of vibration isolation performance using negative stiffness and inerter dampers. J Franklin Inst 2019;356(14):7922–46.

[101] Dwivedi A, Banerjee A, Bhattacharya B. Simultaneous energy harvesting and vibration attenuation in piezo-embedded negative stiffness metamaterial. J Intell Mater Syst Struct 2020;31(8):1076–90.

[102] Banerjee A, Adhikari S, Hussein MI. Inertial amplification band-gap generation by coupling a levered mass with a locally resonant mass. Int J Mech Sci 2021;106630.

[103] Yuksel O, Yilmaz C. Realization of an ultrawide stop band in a 2-D elastic metamaterial with topologically optimized inertial amplification mechanisms. Int J Solids Struct 2020;203:138–50.

[104] Mi Y, Yu X. Sound transmission of acoustic metamaterial beams with periodic inertial amplification mechanisms. J Sound Vib 2021;499:116009.

[105] Adhikari S, Banerjee A. Enhanced low-frequency vibration energy harvesting with inertial amplifiers. J Intell Mater Syst Struct 2021. 1045389X211032281.

[106] Chowdhury S, Banerjee A, Adhikari S. Enhanced seismic base isolation using inertial amplifiers. Structures 2021;33:1340–53. http://dx.doi.org/10.1016/j.istruc.2021.04.089, URL https://www.sciencedirect.com/science/article/pii/S2352012421003908.

[107] Roberts JB, Spanos PD. Random vibration and statistical linearization. Courier Corporation; 2003.

[108] Jimin H, Zhi-Fang F. Modal analysis. Oxford: Linacre House; 2001, OX2 8DP.

[109] Batou A, Adhikari S. Optimal parameters of viscoelastic tuned-mass dampers. J Sound Vib 2019;445:17–28.

[110] Hu Y, Chen MZ, Shu Z, Huang L. Analysis and optimisation for inerter-based isolators via fixed-point theory and algebraic solution. J Sound Vib 2015;346:17–36.